

An analysis of infrared emission spectra from the regions near the Galactic Center

Marcella Contini

School of Physics and Astronomy, Tel Aviv University, Tel Aviv 69978, Israel

Accepted: Received ; in original form 2009 month day

ABSTRACT

We present consistent modelling of line and continuum IR spectra in the region close to the Galactic center. The models account for the coupled effect of shocks and photoionization from an external source. The results show that the shock velocities range between ~ 65 and 80 km s^{-1} , the pre-shock densities between 1 cm^{-3} in the ISM to 200 cm^{-3} in the filamentary structures. The pre-shock magnetic field increases from $5 \cdot 10^{-6}$ gauss in the surrounding ISM to $\sim 8 \cdot 10^{-5}$ gauss in the Arched Filaments. The stellar temperatures are $\sim 38000 \text{ K}$ in the Quintuplet cluster and $\sim 27000 \text{ K}$ in the Arches Cluster. The ionization parameter is relatively low (< 0.01) with the highest values near the clusters, reaching a maximum > 0.01 near the Arches Cluster. Depletion from the gaseous phase of Si is found throughout the whole observed region, indicating the presence of silicate dust. Grains including iron, are concentrated throughout the Arched Filaments. The modelling of the continuum SED in the IR range, indicates that a component of dust at temperatures of $\sim 100\text{-}200 \text{ K}$ is present in the central region of the Galaxy. Radio emission appears to be thermal bremsstrahlung in the E2-W1 filaments crossing strip, however a synchrotron component is not excluded. More data are necessary to resolve this questions.

Key words: Galaxy : center –models : composite (shocks + photoionisation)

1 INTRODUCTION

The Galaxy central region cannot be observed in the optical and UV range because of strong extinction (Erickson et al 1991), but in recent years, infrared observations allowed a detailed investigation of the gas and dust structures.

Fig. 1 shows a radio image of this region (Yusef-Zadeh & Morris 1987). The Sgr A West HII region contains a quiescent black hole $\sim 4 \cdot 10^6 M_{\odot}$ (Ghez et al. 2005; Eisenhauer et al. 2005) which is coincident with the radio source Sgr A* and is located at the center of the Galaxy. It also contains a cluster of massive stars. A distance of 8 kpc is assumed by Simpson et al (2007). Two other clusters of young massive stars and massive molecular clouds (Schödel et al. 2006) appear in the Galactic Center (GC). The Arches Cluster and the Quintuplet Cluster are located $\sim 25 \text{ pc}$ away in the plane of the sky. The Arches Cluster (Nagata et al 1995 and Cotera et al. 1996) is a very massive and dense cluster of young stars heating and ionizing the region of the Arched Filaments and the Sickle. These are thermal radio emitters (e.g. Yusef-Zadeh & Morris 1987, Morris & Yusef-Zadeh 1989, Lang et al. 1997, 2001), while the Radio Arc (Yusef-Zadeh et al 1984) consists of non-thermally emitting linear filaments perpendicular to the Galactic plane. The

stars of the Quintuplet Cluster ionize the clouds in the extended region including the Bubble. A detailed description of the GC is given by Simpson et al (2007).

Excitation of the gas is ascribed to photoionization because it was found that the excitation variations depend on the projected distances from the clusters (Erickson 1991).

The radial velocity field is very complicated. The gas velocity range in the Sickle is $\sim 40\text{-}140 \text{ km s}^{-1}$ (Yusef-Zadeh et al 1997, Lang et al. 1997), and seems lower closest to Sgr A. Interestingly, in both the Arched Filaments and the Sickle the velocity of the molecular clouds is similar to that of the gas.

According to the morphology in Fig. 1, it appears that the cloud structures characterised by a system of semi-circular arcs, arise from stellar winds or supernova explosions. This can be noticed for instance, in the Bubble region (Levine et al. 1999) and in the Radio Arc Bubble (Rodríguez-Fernández et al. 2001). At the same position on the plane of the sky as the Bubble, there is a dense molecular cloud, G0.0110.011 (Tsuboi et al. 1997) or G0.0130.013 (Oka et al. 2001).

Stellar winds and supernova explosions suggest that the shocks have a non-negligible role in heating and ionizing both the gas and the dust. The fragmented filamentary

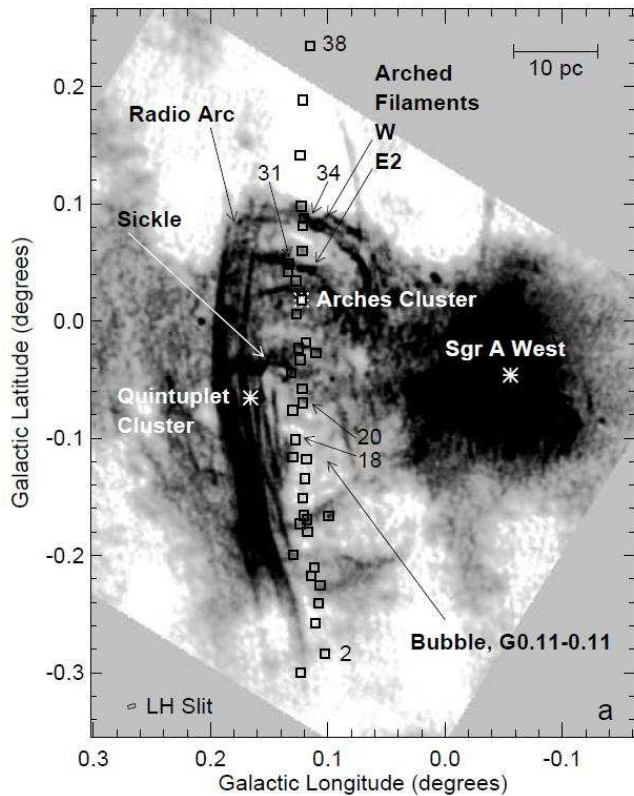


Figure 1. Images of the Galactic Center with the observed positions indicated by square boxes upon the radio continuum (log-log scale) imaged at 21 cm imaged by Yusef-Zadeh & Morris (1987) with 11" resolution (adapted from Simpson et al.2007, Fig. 1.)

structures characteristic of the GC strengthens this hypothesis.

The Arches Cluster has also been investigated in the light of dynamical evolution of compact young clusters (e.g. Kim, Morris, & Lee 1999, Kim et al. 2000).

In the X-ray domain, using the Chandra telescope, Yusef-Zadeh et al. (2002) detected three X-ray components associated with the Arches Cluster. They claim that hot (10^7 K) X-ray emitting gas is produced by an interaction of material expelled by the massive stellar winds with the local interstellar medium. One of the sources has roughly the characteristics expected from shock-heated gas created by the collision of a number of 1000 km s^{-1} stellar winds emanating from the stars in the rich dense cluster. However, the X-ray sources are extended and hardly related to single X-ray binary systems.

Far-infrared (FIR) lines were observed using the Kuiper Airborne Observatory (KAO: Colgan et al. 1996; Simpson et al. 1997) and the Infrared Space Observatory (ISO: Rodríguez-Fernández et al. 2001; Cotera et al. 2005). For both the Arched Filaments (Colgan et al. 1996; Cotera et al. 2005) and the Sickle (Simpson et al. 1997; Rodríguez-Fernández et al. 2001), the excitation decreases with distance from the Arches Cluster and Quintuplet Cluster, respectively, as expected for photoionization.

Spitzer observations of MIR spectra in 38 positions along a line approximately perpendicular to the Galactic plane in the GC are presented by Simpson et al (2007),

who analyse the sources of excitation of the Arched Filaments and of the other thermal arcs. They are particularly interested in the Bubble physical conditions relatively to the clusters and the other filament structures. The observed positions are shown in Fig. 1. Their spectra contain high and low ionization level lines (e.g. [OIV], [SIV], [NeIII], [NeII], [SIII], [FeIII], [FeII], and [SiII]).

In their paper, Simpson et al. (2007) use the new observations to determine the stellar properties of the most massive stars in the Arches Cluster. However, the modelling of the spectral line ratios by pure photoionization codes, (e.g. CLOUDY etc.) was successful only to explain some line ratios in a few positions. Simpson et al. (2007) conclude that the models accounting for the shocks by Contini & Viegas (2001) could explain the relatively strong [OIV] lines. This induced us to revisit Simpson et al. observations of the Galactic central region, by a detailed modelling of the line and continuum spectra, constraining the results by the interpretation of the spectra previously observed by Erickson et al. (1991) and Colgan et al.(1996). We adopt for the calculations the code SUMA which accounts for both photoionization and shocks. In particular, all the lines available in each spectrum and the continuum spectral energy distribution (SED) will be modelled in a consistent way. The results will explain the excitation mechanisms of the gas near the GC as well as some particular features, e.g. the distribution of dust. The calculation details are described in Sect. 2. In Sect. 3 the spectra presented by Simpson et al. are modelled and discussed. In Sect. 4, line and continuum spectra are modelled for Position C - G0.095+0.012 and the E2 thermal radio Filament which were observed by Erickson et al (1991). In Sect. 5 we examine the observations of Colgan et al (1996) in the different positions crossing the E2-W1 arched radio filament. Concluding remarks follow in Sect. 6.

2 THE MODELLING METHOD

The physical parameters are combined throughout the calculation of forbidden and permitted lines (see Osterbrock 1988) emitted from a shocked nebula. Besides the element abundances, the main parameters are known to be : the electron density n_e , the electron temperature T_e , the component of the magnetic field perpendicular to the flow direction B , the flux from the external source, which is characterised by its spectral type (e.g. a black body) and intensity (e.g. the ionization parameter U), and the fractional abundance of the ions. They follow the recombination trend of the gas downstream. Therefore, the precision of the calculations requires to divide the downstream region in many different slabs corresponding to the different physical conditions. The line and continuum intensities in the X-ray - radio range, are calculated in each slab and integrated throughout the nebula geometrical thickness.

In pure photoionization models the density n is constant throughout the nebula, while in a shock wave regime, n is calculated downstream by the compression equation in each of the single slabs. Compression depends on n , B , and the shock velocity V .

The ranges of the physical conditions in the nebula are deduced, as a first guess, from the observed lines (e.g. the

shock velocity from the FWHM) and from the characteristic line ratios (e.g. n_e and T_e).

The observations indicate that a steady state situation can be applied (Cox 1972). In this case, the time t required for a parcel of gas to cross the cooling region from the shock front to the recombination zone, for shock waves with $v=100$ km s^{-1} , is found to be about $1000/n_e$ years (calculated by the recombination coefficients) so, for an electron density $n_e = 100 \text{ cm}^{-3}$, $t = 10$ years. Shock velocities within the GC are not likely to change appreciably in that short a time, so the steady state calculation should be adequate.

In this paper, the line and continuum spectra emitted by the gas downstream of the shock front, are calculated by SUMA (see <http://wise-obs.tau.ac.il/~marcel/suma/index.htm> for a detailed description). The code simulates the physical conditions in an emitting gaseous cloud under the coupled effect of photoionisation from an external radiation source and shocks. The line and continuum emission from the gas is calculated consistently with dust reprocessed radiation in a plane-parallel geometry.

In a composite (shock and photoionization) code such as SUMA, the input parameters are: the shock velocity V_s , the preshock density n_0 , the preshock magnetic field B_0 which refer to the shock, while, the colour temperature of the hot star T_* and the ionization parameter U (the number of photons per number of electrons at the nebula) refer to the flux. The geometrical thickness of the emitting nebula D , the dust-to-gas ratio d/g , and the abundances of He, C, N, O, Ne, Mg, Si, S, A, and Fe relative to H are also considered. The distribution of the grain radius (a_{gr}) downstream is determined by sputtering, beginning with an initial radius.

The calculations start at the shock front where the gas is compressed and thermalized adiabatically, reaching the maximum temperature in the immediate post-shock region ($T \sim 1.5 \cdot 10^5 (V_s/100 \text{ km s}^{-1})^2$). T decreases downstream following recombination. The cooling rate is calculated in each slab. The downstream region is cut up into a maximum of 300 plane-parallel slabs with different geometrical widths calculated automatically, in order to account for the temperature gradient (Contini 1997 and references therein).

In each slab, compression is calculated by the Rankine-Hugoniot equations for the conservation of mass, momentum and energy throughout the shock front. Compression (n/n_0) downstream ranges between 4 (the adiabatic jump) and ≤ 10 , depending on V_s and B_0 . The stronger the magnetic field the lower is compression downstream, while a higher shock velocity corresponds to a higher compression.

The ionizing radiation from an external source is characterized by its spectrum depending on T_* , and by the ionization parameter. The flux is calculated at 440 energies, from a few eV to KeV. Due to radiative transfer, the spectrum changes throughout the downstream slabs, each of them contributing to the optical depth. In addition to the radiation from the primary source, the effect of the diffuse radiation created by the gas line and continuum emission is also taken into account, using 240 energies to calculate the spectrum.

For each slab of gas, the fractional abundance of the ions of each chemical element are obtained by solving the ionization equations. These equations account for the ionization mechanisms (photoionization by the primary and

diffuse radiation, and collisional ionization) and recombination mechanisms (radiative, dielectronic recombinations), as well as charge transfer effects. The ionization equations are coupled to the energy equation when collision processes dominate, and to the thermal balance if radiative processes dominate. This latter balances the heating of the gas due to the primary and diffuse radiations reaching the slab, and the cooling, due to recombinations and collisional excitation of the ions followed by line emission, dust collisional ionization, and thermal bremsstrahlung. The coupled equations are solved for each slab, providing the physical conditions necessary for calculating the slab optical depth, as well as its line and continuum emissions. The slab contributions are integrated throughout the cloud.

In particular, the absolute line fluxes referring to the ionization level i of element K are calculated by the term $n_K(i)$ which represents the density of the ion i . We consider that $n_K(i) = X(i) [K/H] N_H$, where $X(i)$ is the fractional abundance of the ion i calculated by the ionization equations, $[K/H]$ is the relative abundance of the element K to H , and N_H is the density of H (by number cm^{-3}). In models including shock, N_H is calculated by the compression equation (Cox 1972) in each slab downstream (Sect. 2). So the abundances of the elements are given relative to H as input parameters.

Dust grains are coupled to the gas across the shock front by the magnetic field, and are heated by radiation from the stars and collisionally by the gas to a maximum temperature which is a function of the shock velocity, of the chemical composition, and the radius of the grains, up to the evaporation temperature ($T_{dust} \geq 1500$ K). The grain radius distribution downstream is determined by sputtering, which depends on the shock velocity and on the density. Throughout shock fronts and downstream, the grains might be destroyed by sputtering.

Summarizing, very schematically :

- 1) we adopt an initial T_e ($\sim 10^4$ K) and the input parameters;
- 2) calculate the density from the compression equation;
- 3) calculate the fractional abundances of the ions from each level for each element;
- 4) calculate line emission, free-free and free-bound emission;
- 5) recalculate T_e by thermal balancing or the enthalpy equation;
- 6) calculate the optical depth of the slab and the primary and secondary fluxes;
- 7) adopt the parameters found in slab i as initial conditions for slab $i+1$;
- 8) Integrating the contribution of the line intensities calculated in each slab, we obtain the absolute fluxes of each of the lines, calculated at the nebula (the same for bremsstrahlung).
- 8) We then calculate the line ratios to a certain line (in the present case [SIII], because we do not have values of $H\beta$ or other H lines)
- 9) and compare them with the observed line ratios.

The observed data have errors, both random and systematic. Models are generally allowed to reproduce the data within a factor of 2. This leads to input parameter ranges of a few percent. The uncertainty in the calculation results, on the other hand, derives from the use of many atomic parameters, such as recombination coefficients, collision strengths,

etc., which are continuously updated. Moreover, the precision of the integrations depends on the computer efficiency.

Simpson et al. present the spectra observed in close regions throughout the slit. Actually, we are interested in the trend of the physical conditions, as well as in the parameter ranges. Therefore, to avoid the accumulation of errors which leads to inconsistent results, we try to reproduce the data as close as possible. If the calculated lines are compatible with the observed ones within the error of each line, we adopt the input parameters as the result in this observed position. If there are discrepancies, we change consistently the input parameters and we restart the whole calculation process. As explained in the text, the alterations are done on the basis that T_* affects $[\text{NeIII}]/[\text{NeII}]$, U affects $[\text{FeIII}]/[\text{FeII}]$, $[\text{OIV}]/[\text{SIII}]$ depends on V_s , etc. We also change the relative abundances to obtain a good fit for all the line ratios, however, they affect the cooling rate, so it is important to restart the calculation process each time.

As a matter of fact, a degeneracy can arise e.g. from the density and the magnetic field which are directly correlated. There can be a doubt in the values of n_0 and B_0 leading to the best fit of the observations in a certain position p . Our method is to adopt as a first guess, the input parameters of position $p-1$, and then modify them, little by little, calculating a grid of models, until all the observed line ratios in position p are satisfactorily reproduced within the least error.

The number of ionizing photons $\text{cm}^{-2} \text{s}^{-1}$ produced by the hot source is $N = \int_{\nu_0} B_\nu / (h\nu) d\nu$, where $\nu_0 = 3.29 \cdot 10^{15} \text{ s}^{-1}$ and B_ν is the Planck function. The flux from the star is combined with U and n by : $N (r/R)^2 = U n c$, where r is the radius of the hot source (the stars), R is the radius of the nebula (in terms of the distance from the stars), n is the density of the nebula, and c the speed of light. Therefore, T_* and U compensate each other, but only in a qualitative way, because T_* determines the frequency distribution of the primary flux, while U represents the number of photons reaching the nebula. The choice of T_* and U in each position is made by the fit of the line ratios. T_* affects strongly the $[\text{NeIII}]$ line, while $[\text{FeIII}]/[\text{FeII}]$ is more affected by U .

The velocity V and the density n are linked by the continuity equation : $V_0 n_0 = V_1 n_1$. Moreover, B_0 , n_0 , and V_s , are combined in the compression equation (Cox, 1972). In conclusion, all the parameters are combined together in the calculations. Therefore, for each position a large grid of models are run. The models are selected on the basis of the minimum deviation from the observation data for all the line ratios.

3 SPITZER OBSERVATIONS

3.1 The line spectra

Spitzer MIR spectra (Program 3295, all AORs) were observed by Simpson et al. (2007, hereafter S07) in 38 positions along a line approximately perpendicular to the Galactic plane in the GC (Fig. 1). The line intensities were corrected by the $\tau_\lambda/\tau_{9.6}$ optical depth ratios, using the optical depth at $9.6 \mu\text{m}$ $\tau_{9.6}$, as given by S07 in their Table 2 and Table 1 respectively.

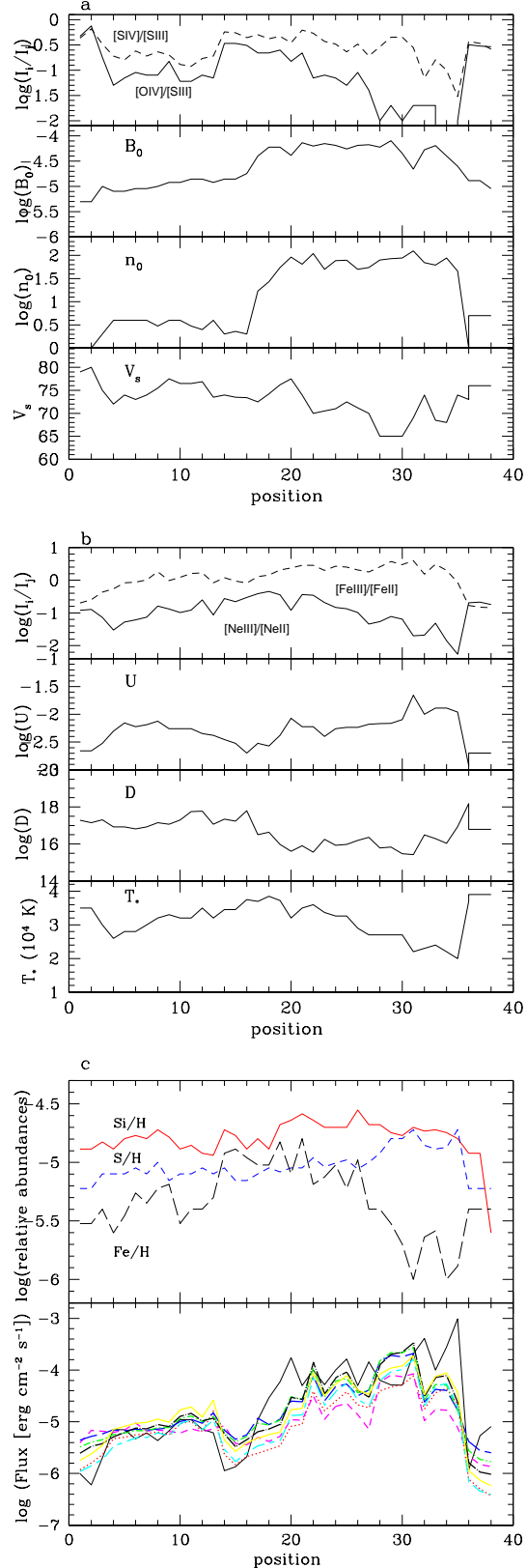


Figure 2. The profiles of the different parameters which result from modelling. a : the parameters depending on the shock; b : the parameters depending on photoionization; c : the relative abundances (top panel); comparison of the continuum fluxes at different wavelength with the calculated bremsstrahlung in the different positions (bottom panel); magenta : 10.0-10.48 μm , blue : 10.5-11.6 μm , red : 12.7-13.8 μm , green : 14.5-15.5 μm , yellow : 16.5-17.5 μm , cyan : 18.5-19.5 μm , black : 20.5-21.5 μm .

In some positions, in particular between 1 and 16, the observed $[\text{SIII}]18.7/[\text{SIII}]33.5$ ratios, corrected for extinction by the $\tau_{9.6}$ presented in S07, were lower than the calculated $[\text{SIII}]18.7/[\text{SIII}]33.5$ lower limit (~ 0.5), even adopting a very low density model. Consequently, the $\tau_{9.6}$ values were incremented in each position in order to lead to a reasonable spectrum. In fact, the $\tau_{9.6}$ values were calculated by Simpson et al (2007) assuming $T_e=6000$ K, while in our models the temperatures downstream, depending on the shock velocity, show higher values in the region close to the shock front (Sect. 3.2.1).

In Table 1, we compare the spectra corrected for extinction with model calculations. In the last column the extinction is given. The spectra are numerated from 1 to 38 referring to S07. Each observed (corrected) spectrum is followed in the next row by the calculated one, which is numerated from m1 to m38. Model m_{pt} which appears in the last row of Tables 1 and 2 is explained in Sect. 3.3.

The models adopt a black body photo-ionizing radiation flux corresponding to the colour temperature of the stars. The model parameters are given in Table 2, where columns 2-4 list the shock parameters. Columns 5 and 6 give the photoionizing flux : the temperature of the stars and the ionization parameter, respectively. The relative abundances Si/H, S/H, and Fe/H follow in columns 7-9. The O/H and Ne/H ratios were found nearly constant in all S07 positions, by a first modelling. In fact, depletion into dust grains is not important since O is not the main constituent of dust grains and Ne cannot be adsorbed due to its atomic structure. The last column shows the geometrical thickness of the emitting filaments. Indeed, a high fragmentation of matter appears in the observed region and in each position, many different conditions could coexist. In our modelling we refer to the data as to single (average) spectra.

In Table 1, we show the line ratios normalized to $[\text{SIII}]33.5=10$ -the strongest line - to avoid very small values. The line sequence is ordered by wavelength. A grid of models was run for each position and the best fitting spectrum was selected on the basis of the $[\text{SIV}]/[\text{SIII}]$, $[\text{NeIII}]/[\text{NeII}]$, and $[\text{FeIII}]/[\text{FeII}]$ flux ratios which do not depend on the relative abundances, and of $[\text{OIV}]/[\text{SIII}]$ which depends strongly on the shock velocity.

To understand the results, we recall that the radiative ionization rates depend on the intensity of the primary and secondary (diffuse) radiation flux; radiation cannot heat the gas to $> 2\text{-}3 \cdot 10^4$ K. The shocks heat the gas to temperatures which depend on the shock velocity and the collisional ionization rates increase with increasing temperatures.

We derive T_* and U by the best fit of $[\text{NeIII}]/[\text{NeII}]$ and $[\text{FeIII}]/[\text{FeII}]$, respectively. However, these parameters also affect $[\text{SIV}]/[\text{SIII}]$. So the whole process is iterated until all the line ratios are reproduced.

The $[\text{OIV}]$ line corresponds to a relatively high ionization level that can be reached collisionally by a relatively high temperature gas, depending on V_s . It was found that the $[\text{OIV}]$ line is hardly detected for shock velocities $< 64 \text{ km s}^{-1}$. Only shocks with $V_s > 64 \text{ km s}^{-1}$ can lead to results suitable to the observations.

The ionization potential of S^{+3} is lower than those of O^{+2} and Ne^{+2} . Therefore, the $[\text{SIV}]$ line intensity depends on U and T_* more than on V_s . Moreover, $[\text{SIV}]/[\text{SIII}]$ decreases with distance from the shock front downstream fol-

lowing recombination, because the S^{+3} region is totally included within the nebula, while the S^{+2} region can be cut off at a certain distance from the shock front in matter-bound nebulae. The geometrical thickness of the emitting cloud is determined when the calculated $[\text{SIV}]/[\text{SIII}]$ line ratio reproduces the observed one. The relative abundance of S is determined by all the line ratios because they are given as ratios to $[\text{SIII}]$. When the line ratios are either all overestimated or all underestimated by the same factor, S/H is modified in order to reproduce the data. S and Si are not strong coolant, therefore Si/H and S/H result directly, without re-starting the whole modelling process.

3.2 Results

The results of modelling are presented in the three diagrams of Fig. 2. a,b,c. We define as *results* the sets of input parameters (V_s , n_0 , B_0 , T_* , U , D , and the relative abundances) which lead to the best fit of the data in each position.

When a cloud moves toward the photoionization source, the shock front edge is reached directly by the photons. When the cloud propagates outwards, the photoionising flux reaches the cloud on the edge opposite to the shock front. Therefore, the calculations need some iterations. In the present modelling, the best fit is obtained considering that the shock front is reached by radiation from the hot stars. This indicates that the clouds move towards the photoionization source. The case of an outward motion was discarded because we could not reach a consistent fit of all the lines in the different positions.

Comparing our results with those generally derived from specific line ratios (e.g. Simpson et al. 2007), we recall that n_0 and B_0 are pre-shock values, while electron densities and temperatures derived from the observed line ratios, refer to the values in the downstream regions.

To illustrate the results, we present in Fig. 3 the profiles of the electron temperature, the electron density, and the fractional abundance of the most significant ions downstream, e.g. for model m18.

3.2.1 The parameters depending on the shock

In Fig. 2a, V_s , n_0 , and B_0 are shown as a function of position. The curves are not smooth, because the matter is strongly fragmented and the calculations refer to *averaged* observations in each position. There is a trend of decreasing V_s from positions 1 to 30, with a fluctuating increase from 30 to 38. The density is minimum between 14 and 16, namely in the Bubble. The abrupt increase in n_0 by a factor ≤ 10 after position 16, leads to relatively high densities up to position 35, which corresponds to the limit of the Arched Filament region. Then the density returns to the values characteristic of the ISM.

The trend of increasing B_0 starts smoothly from position 1 and follows, on a reduced scale, the bump of the density in the Arched Filament region. Considering that line excitation and recombination coefficients, and cooling and heating rates depend on the density of the gas downstream, B_0 and n_0 must be cross-checked in each position.

The magnetic field throughout the regions covered by the slit (Fig. 1) is still under discussion (S07). Yusef-Zadeh

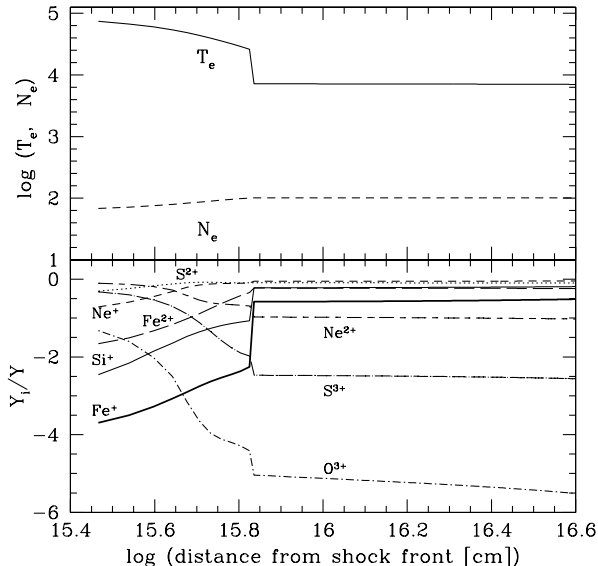


Figure 3. The distribution (top panel) of the electron temperature, the electron density, and (bottom panel) of the fractional abundance of the most significant ions downstream for model m18.

& Morris (1987a) claim that the magnetic field in the linear non-thermal filaments of the Radio Arc is as high as 10^{-3} gauss, while LaRosa et al (2005) found that the global field of the GC is only $\sim 10^{-5}$ gauss with an upper limit of $\leq 10^{-4}$ gauss. The low value is similar to that in the ISM. The consistent modelling of all the lines in each position leads to a growth of B_0 in the arched filament region by a factor of 10 (from $\sim 10^{-5}$ to $\sim 10^{-4}$ gauss), while in the surrounding ISM, B_0 is lower.

In Fig. 2a (top panel), we notice that the observed $[\text{OIV}]/[\text{SIII}]$ line ratio follows the V_s decreasing slope, while $[\text{SIV}]/[\text{SIII}]$ is affected also by the other parameters.

3.2.2 The parameters depending on the radiation flux

In the bottom panel of Fig. 2b, the temperature of the stars, which are the source of the photoionizing flux, is shown as a function of position. A maximum corresponding to $\sim 3.7 \cdot 10^4$ K appears in the region corresponding to the Bubble. These temperatures refer to the Quintuplet cluster. Star temperatures in the Arches Cluster are lower, $\leq 3 \cdot 10^4$ K. We would expect a higher U in the positions closest to the clusters, but 1) we are dealing with projected distances and 2) the geometrical thickness has a crucial role in reducing the photoionization flux throughout the different slabs downstream. Fig. 2b in fact shows that the minimum of U between positions 14 and 20 is accompanied by a rough bump in D .

Fig. 2b shows that the observed $[\text{NeIII}]/[\text{NeII}]$ line ratio is correlated with T_* , while $[\text{FeIII}]/[\text{FeII}]$ is roughly proportional to U .

3.2.3 The relative abundances

The relative abundances resulting from modelling are shown in Fig. 2c (top panel). They are calculated consistently with V_s , n_0 , B_0 , and T_e .

We had some difficulty to determine O/H because the $[\text{OIV}]/[\text{SIII}]$ line ratio could depend on V_s , O/H, and on S/H as well. We decided to keep O/H constant (and Ne/H constant) only after considering a first iteration of results from all the positions and noticing that O/H and Ne/H were changing very little from position to position. The best results were obtained by $\text{O}/\text{H} = 6 \cdot 10^{-4}$ and $\text{Ne}/\text{H} = 10^{-4}$ ($\text{Ne}/\text{O} = 0.167$) and $\text{N}/\text{O} = 0.18$. Grevesse & Sauval (1998) find $\text{Ne}/\text{O} = 0.15$ and $\text{N}/\text{O} = 0.123$. These values are within the range calculated by Martín-Hernández et al (2002) for HII regions in the Galaxy. For elements whose lines were not observed, we adopted the following abundances: $\text{C}/\text{H} = 3.3 \cdot 10^{-4}$, $\text{N}/\text{H} = 1.1 \cdot 10^{-4}$, $\text{Mg}/\text{H} = 2.6 \cdot 10^{-5}$, and $\text{Ar}/\text{H} = 6.3 \cdot 10^{-6}$ (Allen 1973). Thus, they do not appear in Table 2.

Si appears through one only line. Si/H is determined in each position after the satisfactory fit of all the other line ratios. In fact Si is not a strong coolant. The Si/H relative abundance can assume all the values below the solar one ($3.3 \cdot 10^{-5}$), because Si is the main component of silicate grains.

The most impressive result refers to Fe. The strong depletion of Fe from the gaseous phase in the Arched Filament region indicates that iron is quite likely depleted into grains. However, its relative abundance is constrained by both $[\text{FeII}]$ and $[\text{FeIII}]$ lines, and therefore cannot always be derived directly by changing Fe/H.

Small grains are easily sputtered. Iron returns to the gaseous phase at higher V_s close to the Quintuplet Cluster. Si is slightly depleted from the gaseous phase along all the slit positions with some fluctuations, indicating a minimum of silicate grains near the Sickle. Si/H reaches values close to solar in the Arched Filaments beyond the Arches Cluster. Perhaps silicate grains are evaporated by the strong radiation from the cluster. In the Bubble, both Si/H and Fe/H are slightly reduced, indicating that a large fraction of grains survive. Although the IR range observed by Simpson et al. includes the PAH bands observed in the Milky Way (Draine & Li 2007), silicates including iron and other iron species, can also be present in dust. We will discuss these features through the analysis of the continua at different wavelengths which is shown in the bottom panel of Fig. 2c, after modelling the continuum SED in the next section.

3.3 A power-law flux from the Galactic center?

The results in the extreme positions 1-2, 36-38, showing a relatively high T_* , are unusual in the ISM, suggesting that perhaps we should try models which account for a power-law (pl) flux from the center of the Galaxy, as for AGNs (e.g. Contini & Viegas 2001), instead of a black body (bb). In fact, in the Galaxy center there is a "quiescent" BH (Ghez et al. 2005), which is likely not far from the observed positions. We have run a grid of models (m_{pl}) with a pl ionization flux and the other parameters similar to those found by modelling with a bb. The selected model appears in the last row of Tables 1 and 2. Actually, we could not find a fit to the observed line ratios as good as that found by the bb models.

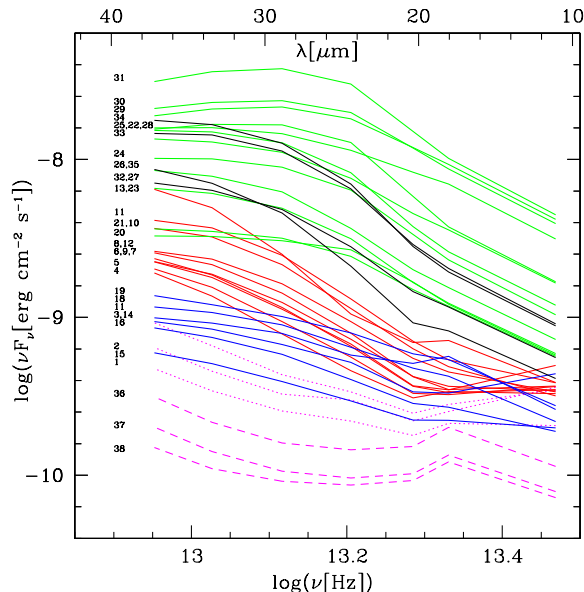


Figure 4. The observed corrected continuum SEDs in the different positions. magenta dotted : 1-3; red solid : 4-13; blue solid : 14-19; green solid : 20-31; black solid : 32-35; magenta dashed : 36-38

In addition, a small contribution of this spectrum would not change the results.

The flux F_ν is lower by at least a factor of 100 than the lowest flux found for LINERS (Contini 1997) and for low luminosity AGN (Contini 2004). Moreover, we found $O/H=8 \cdot 10^{-4}$ and $Ne/H=10^{-4}$.

The best fitting pl model was run with photoionization and shocks acting on the same edge of the cloud, which means that the cloud is propagating towards the (supposed active) center. Inflow is characteristic of regions close to the AGN active center.

3.4 The continuum

We adopt the observational data of the continuum by Simpson et al (2007, Table 4). The data were corrected for extinction by the same correction parameters as those used for the lines (Table 1). The SEDs in the different positions as a function of the frequency are shown in Fig. 4. The error-bands are not included in the figure for the sake of clarity. Two different trends appear : one characteristic of positions in the ISM : 1, 2, 3 (dotted lines) and 36, 37, 38 (dashed lines). The other trend prevails in the other regions (except in position 20). Different colours refer to different groups of positions, in order to have a qualitative view of the SEDs.

3.4.1 The continuum SEDs

To understand the trends in Fig. 4, we present in Fig. 5 the comparison of the continua calculated by the models which were used to calculate the line ratios with the data for position 1, 20, and 31 in a large range of frequencies, from radio to X-ray. Unfortunately, the data cover only the range between ~ 10 and $35 \mu\text{m}$. The calculated continuum SED

shows the contribution of the gas (free-free+free-bound) and that of dust reprocessed radiation, separately.

An interesting result appears from Fig. 5, namely, the dust reradiation peak predicted by the models, which explain the line ratios (solid lines), occurs at a frequency lower than that derived from the observations in positions 20 and 31, while in position 1, model m1 can reproduce the continuum adopting grains with a radius $a_{gr} \sim 0.01 \mu\text{m}$ (dashed lines). Very small grains can be heated stochastically to temperatures (≤ 50 K, Draine 2003) which, however, are not high enough to shift the frequency peak. PAHs correspond to small grains ($\leq 0.01 \mu\text{m}$), while the size of grains including Fe is still under discussion (Hoefner 2009).

Previous calculations of models including dust (Contini et al 2004) show that the peak shifts to higher frequencies 1) increasing V_s i.e. increasing the collisional heating of dust grains, 2) increasing U , i.e. increasing radiation heating of the grains, and 3) reducing the radius of the grains. Excluding collisional heating derived from a higher velocity which would imply very broad line profiles, the only parameters that we can alterate, are U and a_{gr} . We have calculated some models with a very high ionization parameter which represent the case of an emitting cloud closer to the hot source, or less screened from the radiation flux. For positions 20 and 31 we had to use a ionization parameter higher by a factor > 100 than that used for the lines in order to fit the IR continuum data. The model, leading to the hot dust component, produces different line fluxes destroying the nice fit of the line ratios to the data shown in Table 1. So this model contribution corresponds to a low relative weight.

In positions 20 and 31, a dust temperature of ~ 150 K (dashed lines) explains the data in the IR, while dust within the cloud emitting the line spectrum at position 20 reaches only a temperature of ~ 38 K (solid lines). Moreover, Fig. 5 shows that the IR continuum in positions 20 and 31 is emitted by dust while in position 1 the data are reproduced by the sum of reradiation fluxes by dust and bremsstrahlung. This explains the different slopes in Fig. 4. In agreement with very non-homogeneous matter in each observed region, different clouds contribute to the spectra. Alternatively, the relatively hot dust could be spread in the central region of the Galaxy, independently from the gas morphology.

3.4.2 Comparison of IR continuum fluxes

In Fig. 2c (bottom panel) the bremsstrahlung (black solid line) in the IR range *calculated at the nebula* at each position, is compared with the fluxes corresponding to different wavelengths *observed (corrected) at Earth*, in the continuum. They are shifted by a factor η which depends on the distance of the clouds from the photoionization source and on the distance of the clouds to Earth. Adopting a distance to Earth of 8 kpc (Simpson et al 2007), the distance of the dusty clouds from the cluster is ≥ 30 pc. Recall that both the bremsstrahlung and the IR fluxes depend on $n^2 D$ (where n is the density of the emitting gas), while the IR fluxes between 10 and $33.48 \mu\text{m}$ depend also on the gas-to-dust ratios, because they are generally emitted from reprocessed dust. A perfect fit of the bremsstrahlung with the IR observed fluxes is not expected due to the approximations of modelling.

Fig. 2c shows that the bremsstrahlung and the IR fluxes

Table 1. Comparison with models of the observed line intensity ratios ($[\text{SIII}] 33.5 = 10$) corrected for extinction

Position	[SIV]10.5	[NeII]12.8	[NeIII]15.6	[SIII]18.7	[FeIII]22.9	[OIV]25.9	[FeII]26	[SIII]33.5	[SiII]34.8	ext(9.6 μm)
1	0.43	14.94	1.80	5.15	0.27	0.47	1.33	10.00	28.56	1.44
m1	0.43	14.8	1.7	5.29	0.25	0.48	1.2	10.	28.56	
2	0.66	13.50	1.74	5.20	0.41	0.75	1.61	10.00	27.57	2.29
m2	0.7	13.3	1.74	5.29	0.34	0.74	1.77	10.	27.4	
3	0.33	10.63	0.78	5.30	0.38	0.18	0.88	10.00	19.61	2.18
m3	0.33	10.1	0.82	5.3	0.37	0.18	0.83	10.	19.8	
4	0.19	12.36	0.37	5.44	0.31	0.05	0.57	10.00	18.53	2.09
m4	0.184	12.0	0.39	5.47	0.30	0.058	0.59	10.	18.3	
5	0.16	9.04	0.48	5.48	0.45	0.07	0.54	10.00	14.64	2.37
m5	0.16	9.48	0.46	5.5	0.45	0.07	0.44	10.	14.3	
6	0.24	8.57	0.53	5.50	0.60	0.09	0.69	10.00	14.97	2.83
m6	0.25	8.5	0.53	5.47	0.6	0.08	0.67	10.	14.4	
7	0.19	8.43	0.63	5.39	0.50	0.08	0.49	10.00	12.61	2.34
m7	0.19	8.7	0.67	5.48	0.55	0.08	0.47	10.	12.9	
8	0.23	5.78	0.94	5.46	0.58	0.08	0.32	10.00	8.78	2.58
m8	0.23	6.0	0.93	5.4	0.56	0.08	0.25	10.	8.4	
9	0.20	9.26	1.23	5.46	0.83	0.15	0.85	10.00	14.59	2.32
m9	0.21	9.29	1.28	5.46	0.85	0.146	0.7	10.	14.7	
10	0.13	8.20	0.84	5.53	0.38	0.06	0.31	10.00	10.50	2.30
m10	0.13	8.38	0.84	5.45	0.35	0.065	0.3	10.	10.6	
11	0.12	7.44	0.91	5.41	0.42	0.06	0.26	10.00	9.28	2.46
m11	0.12	7.8	0.9	5.38	0.477	0.06	0.278	10.	9.24	
12	0.17	6.09	1.53	5.31	0.42	0.08	0.25	10.00	7.17	2.32
m12	0.17	6.6	1.44	5.35	0.4	0.08	0.25	10.	7.6	
13	0.19	9.51	0.82	5.44	0.52	0.07	0.62	10.00	10.36	2.54
m13	0.19	9.	0.84	5.44	0.54	0.076	0.68	10.	11.3	
14	0.57	6.28	1.74	5.22	1.06	0.34	0.88	10.00	12.54	2.75
m14	0.57	6.47	1.79	5.3	1.1	0.32	0.83	10.	12.5	
15	0.55	9.46	2.10	5.21	1.42	0.34	1.51	10.00	16.91	1.75
m15	0.56	9.1	2.1	5.3	1.47	0.34	1.6	10.	17.2	
16	0.44	8.51	2.54	5.24	1.12	0.31	1.37	10.00	14.10	1.57
m16	0.44	8.7	2.65	5.29	1.19	0.34	1.43	10.	14.1	
17	0.55	7.24	2.81	5.59	0.95	0.22	0.73	10.00	11.75	1.75
m17	0.6	7.6	2.83	5.8	1.	0.23	0.77	10.	11.2	
18	0.42	6.49	2.95	6.05	0.96	0.22	0.66	10.00	8.96	1.74
m18	0.45	6.8	2.86	6.	0.93	0.22	0.69	10.	8.04	
19	0.47	8.74	3.12	7.34	1.91	0.25	0.93	10.00	11.45	1.80
m19	0.47	8.6	3.16	7.32	1.9	0.24	1.16	10.	11.48	
20	0.35	12.04	1.44	10.75	1.45	0.15	0.61	10.00	8.96	2.59
m20	0.34	12.1	1.5	10.7	1.47	0.157	0.69	10.	8.5	
21	0.62	7.50	2.75	7.31	1.67	0.22	0.58	10.00	8.89	2.44
m21	0.62	7.5	2.8	7.3	1.7	0.22	0.55	10.	8.89	
22	0.54	8.00	2.77	9.72	0.75	0.07	0.26	10.00	6.68	3.17
m22	0.54	8.	2.77	9.6	0.76	0.075	0.3	10.	6.63	
23	0.37	7.42	1.55	6.57	0.86	0.08	0.43	10.00	9.53	2.50
m23	0.37	7.5	1.6	6.66	0.83	0.08	0.43	10.	9.3	
24	0.33	8.18	1.20	8.38	1.22	0.07	0.45	10.00	7.83	3.11
m24	0.31	8.3	1.34	8.1	1.2	0.07	0.57	10.	7.6	
25	0.23	8.54	1.15	8.73	0.78	0.05	0.31	10.00	7.50	2.91
m25	0.23	8.6	1.16	8.62	0.75	0.05	0.42	10.	7.7	
26	0.33	8.32	0.86	6.73	1.31	0.09	0.63	10.00	11.93	2.67
m26	0.33	8.34	0.88	6.74	1.35	0.09	0.6	10.	11.84	
27	0.19	8.10	0.37	8.07	0.50	0.04	0.28	10.00	7.52	2.91
m27	0.19	7.8	0.45	7.0	0.50	0.04	0.22	10.	7.7	
28	0.29	7.22	0.39	7.95	0.44	0.01	0.17	10.00	6.33	3.18
m28	0.29	7.3	0.45	7.9	0.44	0.014	0.2	10.	6.3	
29	0.45	5.27	0.41	7.89	0.26	0.02	0.07	10.00	3.39	3.11
m29	0.42	5.	0.46	7.5	0.23	0.02	0.09	10.	3.47	
30	0.45	6.51	0.42	8.78	0.24	0.01	0.08	10.00	3.95	3.12
m30	0.4	6.2	0.42	8.9	0.18	0.01	0.1	10.	3.9	

Table 1 (cont)

Position	[SIV]10.5	[NeII]12.8	[NeIII]15.6	[SIII]18.7	[FeII]22.9	[OIV]25.9	[FeII]26	[SIII]33.5	[SiII]34.8	ext.(9.6 μm)
31	0.28	8.48	0.17	13.05	0.16	0.02	0.04	10.00	2.92	3.40
m31	0.28	8.1	0.2	12.9	0.13	0.02	0.05	10.	2.7	
32	0.07	7.68	0.16	7.98	0.26	0.02	0.17	10.00	6.28	2.51
m32	0.07	7.76	0.15	8.2	0.27	0.02	0.18	10.	6.	
33	0.16	5.37	0.26	7.12	0.28	0.02	0.09	10.00	3.85	3.21
m33	0.16	5.9	0.23	7.14	0.26	0.02	0.07	10.	3.2	
34	0.10	9.18	0.13	9.10	0.14	0.00	0.07	10.00	4.21	3.02
m34	0.10	9.0	0.14	9.36	0.14	0.01	0.078	10.	4.8	
35	0.03	11.02	0.06	7.72	0.13	0.01	0.15	10.00	6.17	2.00
m35	0.03	10.8	0.05	8.	0.13	0.01	0.28	10.	7.2	
36	0.37	12.99	2.67	5.40	0.24	0.32	1.41	10.00	23.54	0.80
m36	0.4	13.2	2.2	5.24	0.3	0.34	1.4	10.	24.	
37	0.34	13.41	2.87	5.48	0.21	0.30	1.39	10.00	23.67	0.42
m37	0.36	13.	2.7	5.5	0.37	0.3	1.3	10.	21.3	
38	0.26	14.82	2.70	5.95	0.187	0.29	1.23	10.00	23.27	0.33
m38	0.27	14.8	2.2	5.6	0.2	0.2	1.	10.	25	
m_{pl}	1.9	12.7	3.4	5.3	0.1	0.36	2.1	10	30	

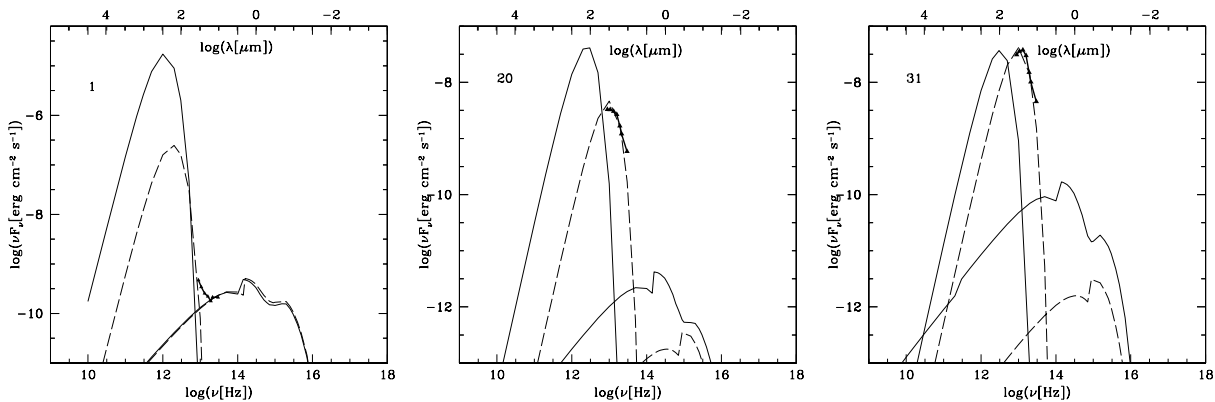


Figure 5. Comparison of calculated with observed SEDs in positions 1, 20, and 31. For each model two curves are shown : one referring to bremsstrahlung peaking at higher frequencies, and one peaking in the IR referring to dust reprocessed radiation. Solid lines : models m1, m20, and m31 calculated by $a_{gr}=0.2 \mu\text{m}$. Dashed lines : in the left diagram correspond to model m1 calculated by $a_{gr}=0.01 \mu\text{m}$, in the middle and right diagrams correspond to models calculated by $U=2.2$.

have roughly similar profiles, except in the ISM positions : in the southern positions, dust reradiation is higher than the bremsstrahlung confirming that that Si, S, and Fe could be depleted from the gaseous phase into grains, while in the northern positions, the dust-to-gas ratios are low.

4 POSITION C - G0.095+0.012 AND THE E2 THERMAL RADIO FILAMENTS

Radio VLA maps show peculiar filamentary structures $\sim 10'$ long located roughly $10'$ northeast of the Galactic center, which suggest fragmentation of matter close to shock fronts. The morphology and the radio polarization (Yusef-Zadeh, Morris, & Chance 1984) indicate that magnetic fields are important, which is significant for models including shocks. Moreover, it was found that the Arches Cluster is photoionizing the region of straight and arched filaments surrounding it (E91). This led us to adopt composite models (shocks+

photoionization) to explain gas and dust spectra observed from both thermal (arched) and non-thermal (linear) structures.

The clouds and filaments at position G0.095+0.012 and the E2 thermal "arched" radio filament near the Galactic center were observed by E91 in 8 positions (Fig. 6). To clarify the nature of these filaments, Erickson et al (1991, hereafter E91) have made FIR line and adjacent continuum observations of [SIII]19, [SIII]33, [OIII]52 and [OIII]88, [NIII]57, [SiII]35, [OI]63, [OI]145, and [CII]158 from NASA's Kuiper Airborne Observatory (KAO). Upper limits were obtained for [SI]25, [FeII]26, and [NIII]36.

In this section the modelling of line and continuum spectra is presented.

Table 2. The models

model	V_s (km s^{-1})	n_0 (cm^{-3})	B_0 (gauss)	T_* (K)	U ¹ -	Si/H -	S/H -	Fe/H -	D (cm)
m1	79	1	5e-6	3.5e4	2.2e-3	1.3e-5	6.e-6	3.e-6	1.92e17
m2	80	1	5e-6	3.4e4	2.1e-3	1.4e-5	7.e-6	5.e-6	1.40e17
m3	75	2	1.e-5	3.e4	3.e-3	1.5e-5	8.e-6	4.e-6	2.e17
m4	72	4	8.e-6	2.6e4	5.e-3	1.3e-5	8.e-6	2.5e-6	8.5e16
m5	74	4	8.e-6	2.8e4	7.e-3	1.6e-5	8.e-6	3.5e-6	8.3e16
m6	73	4	9.e-6	2.8e4	6.e-3	1.7e-5	9.e-6	5.5e-6	6.6e16
m7	74	4	9.e-6	3.e4	6.5e-3	1.6e-5	8.e-6	4.5e-6	8.3e16
m8	75.5	3	1.e-5	3.2e4	7.5e-3	1.9e-5	1.e-5	6.e-6	1.43e17
m9	77.5	4	1.2e-5	3.3e4	5.5e-3	1.65e-5	7.e-6	6.5e-6	1.18e17
m10	76.5	4	1.2e-5	3.2e4	5.5e-3	1.3e-5	8.e-6	3.e-6	1.95e17
m11	76.5	3	1.4e-5	3.2e4	5.5e-3	1.4e-5	8.e-6	4.e-6	5.6e17
m12	76.9	2.5	1.4e-5	3.5e4	4.5e-3	1.2e-5	9.e-6	4.e-6	6.e17
m13	73.5	4	1.2e-5	3.2e4	4.2e-3	1.15e-5	8.e-6	5e-6	1.18e17
m14	74	2	1.4e-5	3.45e4	3.5e-3	1.9e-5	9.e-6	1.2e-5	2.2e17
m15	73.5	2.3	1.4e-5	3.45e4	3.e-3	1.7e-5	7.e-6	1.3e-5	1.7e17
m16	73.4	2	1.8e-5	3.75e4	2.e-3	1.3e-5	7.e-6	1.1e-5	6.3e17
m17	72.5	17	4.e-5	3.7e4	3.e-3	1.6e-5	8.e-6	9.5e-6	3.16e16
m18	74.2	27	6.e-5	3.85e4	2.7e-3	1.3e-5	9.e-6	9.5e-6	4.3e16
m19	76.2	55	6.e-5	3.72e4	4.2e-3	2.1e-5	8.3e-6	1.5e-5	9.5e15
m20	77.5	92	4.1e-5	3.2e4	8.5e-3	2.3e-5	9.e-6	8.e-6	4.e15
m21	74	65	7.3e-5	3.5e4	6.e-3	2.6e-5	9.e-6	1.6e-5	8.e15
m22	70	110	6.3e-5	3.6e4	6.e-3	2.3e-5	1.1e-5	6.5e-6	3.6e15
m23	70.5	50	7.e-5	3.37e4	4.e-3	2.e-5	9.2e-6	7.5e-6	1.8e16
m24	71	77	6.5e-5	3.26e4	5.5e-3	2.e-5	9.9e-6	9.5e-6	8.6e15
m25	72.5	79	5.5e-5	3.26e4	5.8e-3	2.e-5	1.05e-5	6.e-6	9.5e15
m26	71.2	50	6.5e-5	2.9e4	5.8e-3	2.8e-5	8.8e-6	1.05e-5	1.57e16
m27	70	55	6.7e-5	2.7e4	6.6e-3	2.1e-5	1.0e-5	4.e-6	2.3e16
m28	65	80	6.e-5	2.7e4	6.8e-3	2.1e-5	1.2e-5	4.e-6	6.1e15
m29	65	85	8.e-5	2.7e4	6.9e-3	1.8e-5	1.6e-5	3.e-6	6.9e15
m30	65	88	4.5e-5	2.7e4	8.e-3	1.7e-5	1.6e-5	2.e-6	3.e15
m31	69	125	2.2e-5	2.2e4	2.2e-2	2.e-5	1.9e-5	1.e-6	2.7e15
m32	74	70	5.3e-5	2.3e4	1.e-2	1.85e-5	1.4e-5	2.3e-6	3.1e16
m33	68.5	62	6.4e-5	2.4e4	1.3e-2	1.9e-5	1.3e-5	2.6e-6	1.95e16
m34	68	88	4.e-5	2.2e4	1.3e-2	1.8e-5	1.35e-5	1.e-6	1.1e16
m35	74	46	2.5e-5	2.e4	1.1e-2	1.6e-5	1.9e-5	1.3e-6	8.7e16
m36	73	1	1.3e-5	3.7e4	1.2e-3	1.2e-5	6.e-6	4.e-6	1.5e18
m37	76	5	1.3e-5	3.9e4	2.e-3	1.2e-5	6.e-6	4.e-6	6.2e16
m38	76	5	9.e-6	3.9e4	2.e-3	2.5e-6	6.e-6	2.5e-6	5.4e16
<i>m_{pl}</i>	75	3	2.e-6	$\alpha=-2$	$F_\nu=1e6^2$	8.e-6	3.e-5	3.e-6	4.2e16

¹ U is a number² in photons $\text{cm}^{-2} \text{s}^{-1} \text{eV}^{-1}$ at the Lyman limit.

4.1 Position C

4.1.1 The line spectrum

We have corrected the spectrum from extinction as indicated by E91. In Table 3, we compare our models with the observed corrected line ratios normalized to $[\text{SIII}]33.5 = 1$. The best fit is obtained adopting $T_* = 24,000 \text{ K}$ and $U=4 \cdot 10^{-3}$, $V_s = 65 \text{ km s}^{-1}$, and $n_0=200 \text{ cm}^{-3}$. The magnetic field $B_0 = 2 \cdot 10^{-5} \text{ gauss}$ is similar to that found in S07 position 31. The relative abundances which lead to the best fit of the observed spectrum, show that C/H is lower than solar by a factor of 1.65, while N/H is higher by a factor of 1.5. Si, S, and Fe are lower than solar suggesting that they are trapped into grains. Also in this case the clouds are moving towards the hot source, i.e. the Arches Cluster. In our models, the temperature of the stars (24000 K) results phe-

nomenologically because leading to the consistent fit of all the lines. E91 adopted a $T_{\text{eff}}=35,000 \text{ K}$ atmosphere from Kurucz (1979). The LTE atmosphere has a very different UV SED from a black body (Simpson et al 2004, Fig. 6) so the entire modelling is different.

In Fig. 7 we show the profile of the electron temperature and electron density, and of the fractional abundance of the most significant ions downstream as calculated by model *m_C*. The model is matter bound.

4.1.2 The continuum SED

We try to constrain the model adopted to explain the line spectrum, using the SED of the continuum. We plot in Fig. 8 the data from E91. The data cover only the far-IR range,

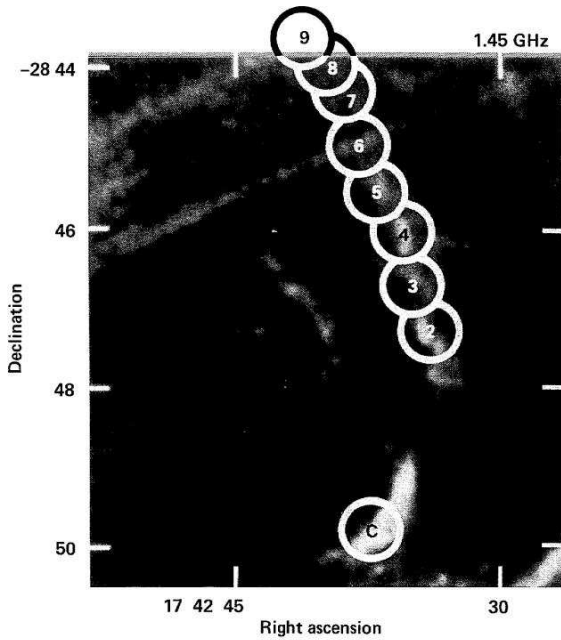


Figure 6. Location of infrared observations overlaid on a VLA continuum radiograph (Yusef-Zadeh et al. 1984). The figure is taken from Erickson et al (1991, Fig. 1).

Table 3. IR line spectrum at position C

line	obs ¹	$I_\lambda/I_{[\text{SIII}]33.5}$ ²	m_C
[SIII] 18.8	21.3±4.0	1.8	1.82
[FeII] 26	<9.4	<0.2	0.2
[SIII] 33.5	70.5 ±1.1	1.	1.
[SIII] 34.8	31.5 ±1.2	0.42	0.41
[NeII] 36.	<0.7	<0.009	0.009
[OIII] 51.8	12.8±0.4	0.135	0.14
[NIII] 57.3	15.7±0.5	0.159	0.15
[OI] 63.2	5.2±0.4	0.05	0.06
[OIII] 88.4	11.2±0.3	0.1	0.08
[OI] 145.5	0.5±0.05	0.004	0.003
[CII] 157.7	8.2±0.1	0.074	0.075
H_β (erg cm ⁻² s ⁻¹)	-	-	6.4e-5
V_s (km s ⁻¹)	-	-	65
n_0 (cm ⁻³)	-	-	200
B_0 (10 ⁻³ gauss)	-	-	0.02
T_* (K)	-	-	2.4e4
U	-	-	4.e-3
D (10 ¹⁴ cm)	-	-	9.7
C/H	-	-	2.0e-4
N/H	-	-	1.5e-4
Si/H	-	-	4.0e-6
S/H	-	-	1.0e-5
Fe/H	-	-	2.6e-6

¹ 10⁻¹⁸ W cm⁻²

² extinction corrected (Erickson et al (1991, Table 1)

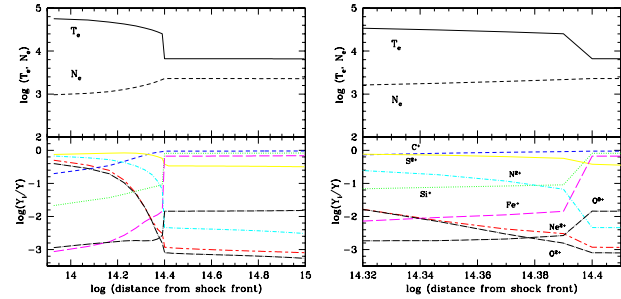


Figure 7. Top : the profile of the electron temperature and the electron density downstream in position C, calculated by model m_C . Bottom : the profile of the fractional abundance of the most significant ions. The diagram on the right presents a zoom of the temperature drop region downstream.

but they are enough to show that with model m_C the continuum data are not reproduced. In particular, the model dust reradiation peak is shifted at a lower frequency. We check whether a higher V_s could improve the agreement since higher V_s lead to higher dust peak frequencies. We have adopted a rather large V_s compared with the radial velocities ($\sim 10 \text{ km s}^{-1}$) measured by E91. Morris & Yusef-Zadeh (1989) suggest a mechanism to account for the ionization and radio emission based on a retrograde, high velocity of $\sim 100 \text{ km s}^{-1}$ cloud encountering the poloidal magnetic field in the vicinity of the GC. Even with such a high velocity, the dust peak could not be reproduced.

In relatively low shock-velocity regimes, a high flux dominates the ionization and heating processes. We have therefore run a model with a very high U ($=5$), as we have done for the dust peak relative to the S07 observations. The other parameters are the same as those of model m_C . The fit to the IR data by the hot dust model is satisfactory. Dust is not homogeneously distributed throughout the observed region. Dilution of U can be explained by a larger distance from the photoionizing source and/or by obscuring matter between the radiation source and the emitting clouds.

4.2 The E2 arched filament

E91 reported the observations of the [SIII]33, [OIII]52, and [OIII]88 lines at eight positions along the E2 arched filament. They claim that the E2 filament is roughly tubular with a 10:1 length to diameter ratio. Moving northward along the filament, the excitation decreases slowly and the line and continuum brightness decrease by a factor of ~ 2 .

In Table 4 we compare the calculated [OIII]52/[SIII]33 and [OIII]52/[OIII]88 line ratios with the data corrected for extinction. The lines observed are too few to fully constrain the models. In Table 4 we refer to positions 2, 4, 6, and 8, where both the [OIII]52 and [OIII]88 lines are observed. We notice by modelling that the line ratios depend strongly on the preshock density. These ratios are significant because [SIII] refers to a ionization potential lower than that of [OIII], so the trend of the [OIII]52/[SIII]33 ratio eventually resembles that of the [OIII]/[OII] ratio, assuming constant relative abundances.

In Fig. 9 the continuum SED in position 2 is compared with the IR data (E91, Table 2) corrected for extinction.

Table 4. IR line spectra in the E2 arched filament

line ratios	position 2		position 4		position 6		position 8	
	obs	calc	obs	calc	obs	calc	obs	calc
[OIII]52/[SII]33	0.176	0.178	0.105	0.105	0.0664	0.067	0.076	0.076
[OIII]88/[SII]33	0.116	0.112	0.079	0.079	0.076	0.076	0.067	0.066
n_0 (cm^{-3})	-	160	-	110	-	40	-	80

for all positions $V_s = 65$ kms, $B_0 = 2 \cdot 10^{-5}$ gauss $U = 4 \cdot 10^{-3}$, $T_* = 24\,000$ K and the relative abundances as for position C.

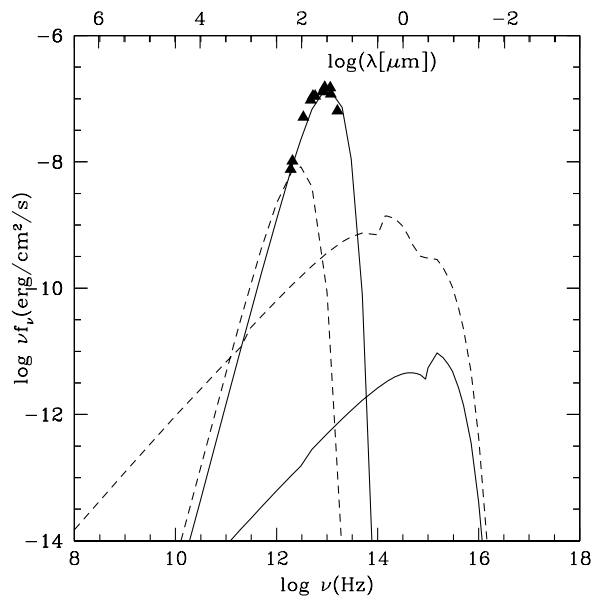


Figure 8. The comparison of the calculated continuum SED in position C with the data (Erikson et al. 1991). Short-dash : model m_C ; solid : model calculated with $U=5$ For all models two curves appear referring to the bremsstrahlung and to reradiation by dust

Using the model which leads to the best fit of the line ratios, dust reaches a maximum temperature of ~ 40 K, while the data are better explained by a temperature of ~ 94 K. This relatively high temperature can be achieved by a very high U (see Sect. 3.3.1). The model which explains the line ratios is constrained by the datum in the radio range. The contribution of the high U cloud component in the line spectra is $< 5\%$. The high U clouds can be very close to stars embedded within the filament, or they are directly reached by radiation from the Arches Cluster stars, as previously explained.

Notice that iron is highly depleted from the gaseous phase, therefore we can attribute IR radiation to iron rich grains (see Sect. 3.3.2).

5 THE SPECTRA IN THE E2-W1 CROSSING STRIP

The region $0^\circ.25$ north of the GC is characterised by ≥ 30 pc long, thin, straight filaments of ionized gas which cross the Galactic plane at right angles (Yusef-Zadeh et al. 1984, Simpson et al. 1997). Their radio continuum emission is polarized and nonthermal, indicating relative strong magnetic

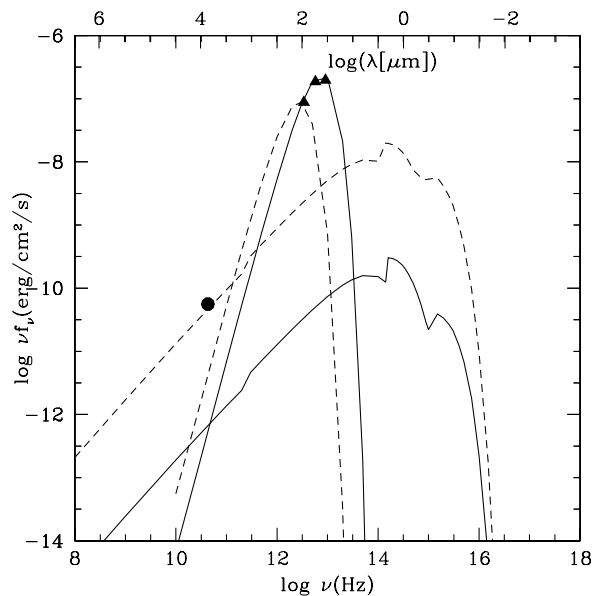


Figure 9. The comparison of the calculated continuum SED with the data in position 2 of the E2 strip (Erikson et al. 1991). Short-dash : model calculated in position 2 (see Table 4); solid : model calculated with $U=5$ For each model two curves appear, one refers to the bremsstrahlung, the other peaking in the IR referring to the dust reprocessed radiation

fields (e.g. Tsuboi et al 1985). In the north-western region, the linear filaments crossing the Galactic plane intersect the Arched filaments, which emit thermal radio continuum. It seems that the linear and arched filaments are connected (Yusef-Zadeh & Morris 1988). The excitation mechanisms responsible for the emission for both sets of filaments is controversial (Colgan et al 1996, hereafter C96, and references therein). Photoionization from Sgr A West is excluded because the photon flux is too low. Photoionization by a line of OB stars close to the filaments is not suitable to the region's morphology. Collisional excitation of the lines, derived from the MHD model of Morris & Yusef-Zadeh (1989) is rejected on the basis of electron densities lower than that of the adjacent molecular gas. Also embedded evolved stars not associated with the filaments could provide some fraction of the continuum, however, Genzel et al (1990) claim that their luminosity is too low to provide the infrared continuum.

It is now clear that the hot young star cluster (the Arches Cluster, Figer et al 1999) found by Cotera et al (1996) and Nagata et al. (1995) is the main source of photoionization. Moreover, the FWHM of the lines presented by Cotera et al. (2005) for the E1 filament and the top of the

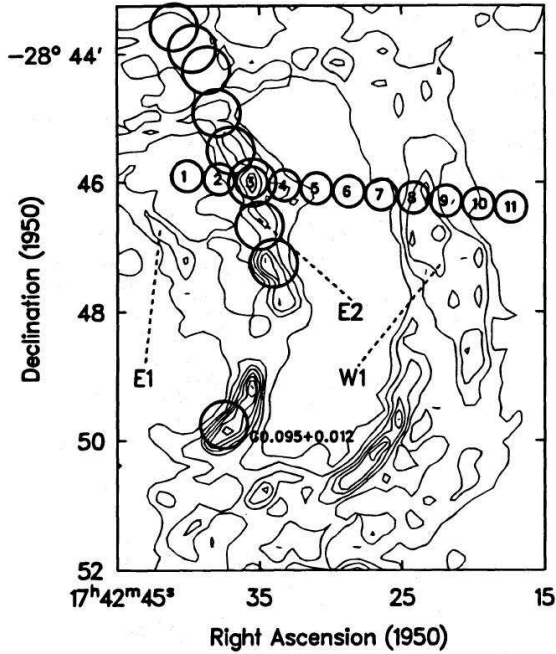


Figure 10. Positions of infrared observations overlaid on a VLA 5 GHz continuum map from the data of Morris & Yusef-Zadeh (1989). (Taken from Colgan et al. 1996, Fig. 2)

E2 filament are relatively high and indicate that the effect of shocks is non negligible.

C96, in their Table 1, present the far-IR line and continuum spectra in 11 positions of the strip between E2 and W1 thermal radio filaments in the Galactic Center "arch" (Fig. 10). In the following we will try to explain the spectra by composite models that were used previously in Sects. 3 and 4, namely, shock and photoionization are consistently adopted to calculate the line ratios. Comparison of calculated with observed line ratios leads to the set of parameter which best describe the physical conditions in the observed regions. We consider that the photoionizing radiation flux is provided by the stars in the Arches Cluster.

The observations were made by the Kuiper Airborne Observatory (KAO) facility Cryogenic Grating Spectrometer (CGS) (Erickson et al. 1985). The lines fluxes presented by C96, include [SIII]33, [SiII]35, [OIII]52, [OI]63, [OIII]88, and [CII]158.

5.1 Preliminary model investigation

Before trying a detailed modelling of the line ratios, we investigate the parameter ranges and their influence on the different line ratios by comparing the observed line ratios with a grid of models in the Fig. 11 plots. The models (mp1-mp10) are described in Table 5. They are characterized by the shock velocity V_s , the pre-shock density n_0 , the ionization parameter U , and a range of geometrical thickness of the clouds which are indicated by point symbols throughout the model trends. In this first trial we adopted a relatively high T_* (34000K) close to that indicated by E91. For all the models $B_0=3 \cdot 10^{-5}$ gauss except for m10 which was calculated by $B_0=10^{-4}$ gauss. A stronger magnetic field prevents the compression downstream which is generally regulated

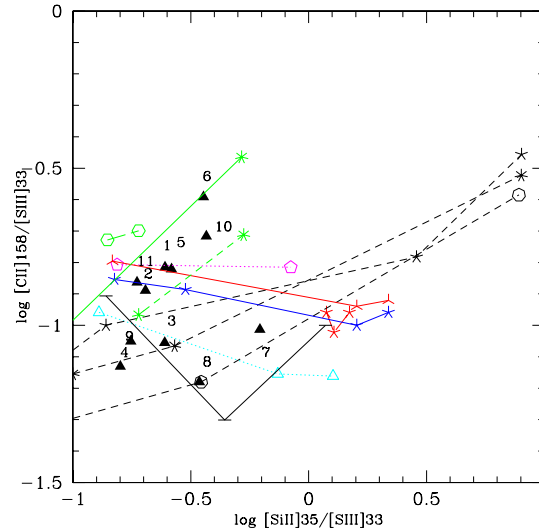
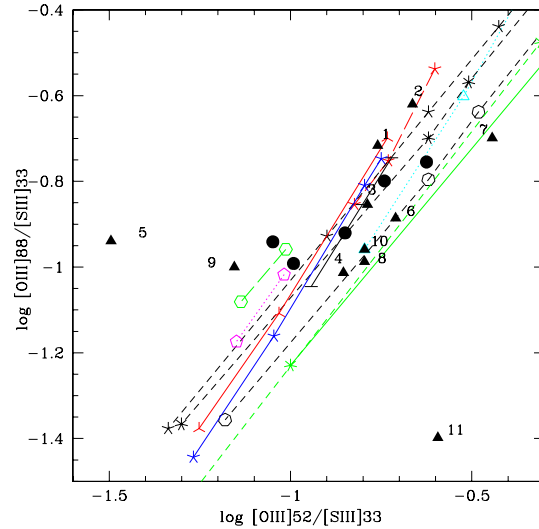


Figure 11. The comparison of model calculations with the the most significant line ratios observed in the E2-W1 crossing strip. The numbers refer to positions in Colgan et al. 1996, fig. 2. The observations are represented by black triangles. In the top diagram we have plotted the data (black dots) from the observations of Erickson et al (1991, Table 2) The models are described in Table 5 and in the text

by the shock velocity and the pre-shock density and leads to unsuitable line ratios.

On the top of Fig. 11, [OIII]88/[SIII]33 versus [OIII]52/[SIII]33 is compared with model results. The data from C96 (their Table 1) are shown as filled triangles. On the same diagram we have plotted the data from the observations of Erickson et al (1991, Table 2) from G0.095+0.012 and the E2 thermal radio filament. The data are distributed from left to right : 6, 8, 4, C, and 2.

This diagram is related to the physical conditions in the gas emitting the lines from the second ionization level. It seems that both the [OIII]88/[SIII]33 and [OIII]52/[SIII]33 ratios increase with increasing density, because the S^{++} region downstream is more reduced than the O^{++} one at

Table 5. The preliminary models

model	V_s (km s^{-1})	n_0 (cm^{-3})	U -	D (10^{15} cm)	symbols
mp1	50	70	0.005	1-10	dotted line linking empty triangles (cyan)
mp2	60	80	0.0005	0.5-50	short-dashed + asterisks (5) (black)
mp3	60	100	0.0005	0.3-30	short-dashed + asterisks(7) (black)
mp4	60	150	0.0005	0.2-16	short-dashed + empty circles (black)
mp5	50	70	0.001	1-2	dotted + empty pentagons (magenta)
mp6 ¹	30	30	0.0015	2-10	long-dashed + empty hexagons (green)
mp7	50	60	0.002	10-100	solid + asterisks (3) (red)
mp8	50	70	0.002	0.8-14	solid + asterisks (5) (blue)
mp9	50	80	0.0015	0.6-4.5	solid + dash (black)
mp10 ²	60	60	0.002	30-150	long dashed + asterisks (5)(red)

¹ m9 was calculated adopting $\text{Si}/\text{H} = 3.3 \cdot 10^{-6}$

² m10 was calculated adopting $B_0=10^{-4}$ gauss

higher n . These ratios are particularly correlated with the geometrical thickness of the filaments, decreasing at higher D .

To constrain the models, we show in Fig. 11 (bottom) the $[\text{CII}]158/[\text{SIII}]33$ vs. $[\text{SiII}]35/[\text{SIII}]33$ plot. The two spectra at positions 5 and 11 which were not reproduced by the models in the top diagram are well included among the other positions in the bottom one. In fact, the spectrum in position 5 shows an unreliable $[\text{OIII}] 52$ (0.5 ± 0.4) and that in position 11 shows an unreliable $[\text{OIII}] 88$ (0.2 ± 0.3). In the bottom diagram which is independent from these lines, the two spectra regain the "normal" trend. We refrain from showing the error-bars in the diagrams for sake of clearness.

The spectra at positions 6 and 10 are not reproduced by the grid of models presented in Table 5. In fact, the relatively high T_* maintains the gas ionized to the second ionization level in a large region, leading particularly to underpredicted $[\text{CII}]/[\text{SIII}]$ line ratios. Cross-checking the results obtained by a detailed modelling of the data (Tables 6 and 7), models mc6 and mc10 (green lines, solid and short-dashed, respectively) were plotted on Fig. 11. Two main trends can be noticed in the bottom diagram. In fact, the combination of the input parameters leads to the stratification of the ions downstream of the shock front, which is also reached by the photoionization flux from the stars (Figs. 3, 7, and 12). For instance, a relatively high T_* and/or a high U maintain the gas ionized to a higher D (the distance from the shock front), while a higher n speeds up recombination because the cooling rate is $\propto n^2$. The shock velocity yields compression (increasing n) and a relatively high temperature downstream ($\propto V_s^2$) leading to a characteristic stratification of the physical conditions. When T_* and/or U are relatively low and D relatively large, the fractional abundance of S^{++} is low and the $[\text{SIII}]$ line flux remains nearly constant at larger D throughout the filament. On the other hand, the first ionization potential of Si and C (8.11 eV and 11.20 eV, respectively) are lower than that of H (13.54 eV), so Si and C remain singly ionized at larger D . This leads to $[\text{CII}]/[\text{SIII}]$ and $[\text{SiII}]/[\text{SIII}]$ line ratios increasing with D . When T_* and/or U are relatively high (models mp1-mp10) and D are such that S^{++} and C^+ fractional abundance are still increasing, $[\text{CII}]/[\text{SIII}]$ slightly decreases. As soon as

D reaches the S^{++} recombination distance, $[\text{CII}]/[\text{SIII}]$ increases. $[\text{SiII}]/[\text{SIII}]$ has an increasing trend because of its very low ionization potential.

To better understand the trend of the models presented in Table 5, the profiles of the electron temperature, of the electron density, and of the fractional abundance of the more significant ions downstream are shown in Fig. 12 for models mp7, mp8, mp6 and mp3 from left to right, respectively. Compression is relatively small for $V_s < 100 \text{ km s}^{-1}$. The best fitting models are matter bound as can be guessed from the relatively low $[\text{SiII}]/[\text{SIII}]$ line ratios.

Summarizing, the trend of the data in the E2-W1 strip was recovered using models with $T_* = 27000\text{K}$. We conclude that, also on the basis of the conditions found in position C ($T_* = 24000\text{K}$) a relatively low temperature is more suitable to the stars close to the observed positions.

5.2 Detailed modelling

The absolute flux of the $[\text{SIII}]33$ line is the strongest one so we will consider line ratios to $[\text{SIII}]$. The ratios of the observed corrected lines fluxes to $[\text{SIII}]33$ are reported in Table 6. The line fluxes were corrected according to C96 factors. The results of modelling are given in the row below that containing the data, for all positions. The selected models numerated from mc1 to mc11 are described in Table 7.

The modelling is constrained by the $[\text{OIII}]/[\text{OI}]$ line ratio, which depends strongly on the ionization parameter, while the $[\text{OIII}]52/[\text{OIII}]88$ ratio depends on the density. The shock velocity is not strongly affecting the line ratios, because lines from relatively high ionization levels were not reported. So we have chosen, as a first guess, V_s in the range of the shock velocities explaining the spectra observed by S07 (Table 2) in the region between E2 and W1. The ranges of the other parameters, n_0 , B_0 , and U , were suggested by the preliminary investigation (Sect. 5.1) which also leads to relatively low T_* .

All the results presented in Table 6 were consistently calculated. In position 5 the density adopted to explain the very low $[\text{OIII}]52/[\text{OIII}]88$ line ratio is exceptionally low. This was already realized by C96. Even by $n_0=10 \text{ cm}^{-3}$, the calculated value is lower than the observed one. Notice,

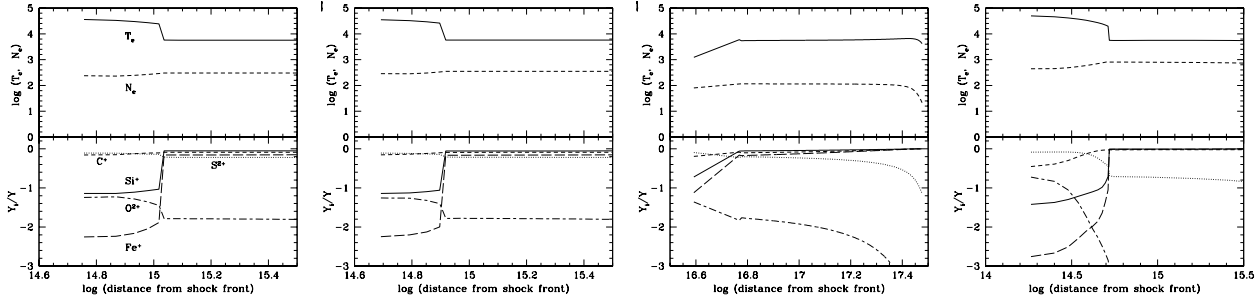


Figure 12. The profile of the electron temperature and of the electron density (top diagrams) and the distribution of the fractional of the most significant ions (bottom diagrams) throughout a cloud corresponding to models (Table 5) mp7, mp8, mp6, and mp3, from left to right, respectively

Table 6. Comparison of observed (corrected) with calculated IR line ratios

Position	[SIII]33	[SiII]35	[OIII]52	[OI]63	[OIII]88	[CII]158
1	10.	2.46	1.29	0.15	1.26	1.53
mc1	10	2.66	1.3	0.2	1.26	1.44
2	10.	2.03	1.61	0.00	1.58	1.29
mc2	10.	2.1	1.63	0.1	1.58	1.26
3	10.	2.45	1.21	0.15	0.94	0.88
mc3	10.	2.4	1.28	0.14	0.93	0.86
4	10.	1.59	1.04	0.32	0.64	0.74
mc4	10.	1.59	1.03	0.31	0.66	0.79
5	10.	2.62	0.24	0.44	0.76	1.51
mc5	10.	2.77	0.46	0.43	0.76	2.36
6	10.	3.58	1.44	-0.45	0.85	2.56
mc6	10.	3.8	1.44	0.42	0.85	2.5
7	10.	6.21	2.65	1.06	1.34	0.97
mc7	10.	6.4	2.54	0.96	1.4	1.06
8	10.	3.44	1.19	-0.08	0.68	0.66
mc8	10.	3.2	1.2	0.085	0.67	0.6
9	10.	1.76	0.52	0.10	0.66	0.89
mc9	10.	1.73	0.52	0.10	0.66	0.9
10	10.	3.68	1.19	0.46	0.74	1.92
mc10	10.	3.5	1.17	0.47	0.73	1.4
11	10.	1.87	1.89	1.22	0.26	1.37
mc11	10.	2.0	1.6	1.29	0.8	1.38

Table 7. The models adopted in the E2-W1 strip

model	V_s	n_0	B_0	U	Si/H	S/H	C/H	D
mc1	65	91	6.e-5	2.e-3	4.e-6	1.3e-5	3.5e-4	2.9e15
mc2	65	91	6.e-5	2.5e-3	4.e-6	1.3e-5	3.5e-4	2.3e15
mc3	65	150	7.e-5	3.0e-3	5.e-6	3.5e-5	3.5e-4	1.7e15
mc4	65	170	5.e-5	2.3e-3	2.7e-6	1.5e-5	3.3e-4	1.35e15
mc5	73	10	8.e-5	8.e-4	5.e-6	4.e-5	9.e-5	2.7e18
mc6	75	190	5.e-5	1.2e-3	1.6e-6	1.e-5	3.3e-4	2.9e15
mc7	70	280	5.e-5	1.9e-3	6.e-6	1.e-5	2.8e-4	9.e14
mc8	70	150	5.e-5	7.e-3	9.e-6	1.2e-5	3.4e-4	1.9e15
mc9	70	30	5.e-5	3.e-3	2.3e-6	1.2e-5	9.e-5	7.3e16
mc10	70	140	3.e-5	3.5e-3	3.9e-6	1.e-5	4.e-4	1.6e15
mc11	70	200	1.e-5	3.1e-3	1.8e-6	1.e-5	3.6e-4	9.0e14

For all models $T_* = 2.7 \cdot 10^4$ K is adopted

however, that the error given by C96 in their Table 1 for the [OIII]52 observed line flux is $\sim 80\%$.

The results are shown in Fig. 13. In Fig. 13a the parameters depending on the shock are given as a function of position. The preshock density shows two deep minima, at positions 5 and 9. As expected, the shock velocity has a maximum in position 5 denoting that the shock velocity range is relatively large. The pre-shock magnetic field shows a decreasing trend in agreement with the results for B_0 obtained by explaining S07 observations between positions 31 and 34. In Fig. 11a the [OIII]88/[OIII]52 ratio shows a profile similar to that of the density, while the radio distribution taken from C96 and shown in the top panel, is not well correlated with the density. This can be explained by recalling that radio and line emissions occur from different regions of the gas downstream in each cloud.

Interestingly, the distribution of both the radio fluxes at 43 and 1.4 GHz shows that the two maxima do not correspond exactly to the maxima in D (Table 6) of $2.7 \cdot 10^{18}$ cm in position 5 and $7.3 \cdot 10^{16}$ cm in position 9.

In Fig. 13b, the profile of U is shown and compared with the observed [OIII]52/[OI]63 and [SII]35/[CII]158 line ratios (top panel). The oxygen line ratio follows the trend of U . The two U minima in positions 5 and 9 correspond to the minima in n_0 . The opposite would be expected because the ionization parameter is reduced by crossing regions of dense gas. This indicates that the origin of the U minima in both positions 5 and 9, is different.

In Fig. 13b (bottom panel) the relative abundances are shown for Si, S, and C, showing that carbon is depleted from the gaseous phase at positions 5 and 9. Then, carbon grains, most probably PAH, screen the flux from the hot source and the radiation flux does not lead to full evaporation of the grains. Also, Si is trapped into dust grains because it shows depletion from the gaseous phase along all the strip.

The other relative abundances adopted by the models are $N/H = 10^{-4}$, $O/H = 6 \cdot 10^{-4}$, and $Ne/H = 10^{-4}$.

In Fig. 14a we present the continuum SED in position 2. The diagram on the left shows the modelling of the data. The short-dashed lines show the bremsstrahlung and dust reradiation calculated by model mc2 which best fit the line ratios. The data in the IR (C96, Table 1) are not well reproduced by the model and indicate that dust grains are heated to a higher temperature, because the dust reradiation maximum is shifted towards higher frequencies. This result was found previously modelling the data by S07 and E91. The best fit is obtained increasing U by a factor of 2000 and reducing a_{gr} to $0.01 \mu\text{m}$. This leads to a maximum dust grain temperature of 88 K. In order to reduce the contribution of such a dusty cloud to the line spectra, a $d/g = 0.4$ by mass is adopted. Grains are neither destroyed by evaporation nor sputtered because the stars are not hot enough and the shock velocities are relatively low, respectively. It seems that these grains are not explained by PAHs because C is not depleted from the gaseous phase in position 2. They could be explained by eroded silicates and/or iron species.

The slope of the radio continuum is an interesting issue. In fact, the non-thermal or thermal character of the emitting clouds is determined on the basis of radio observations. The non-thermal character of the radio emission should confirm the presence of shocks. Synchrotron radiation, created by the Fermi mechanism at the shock front, is

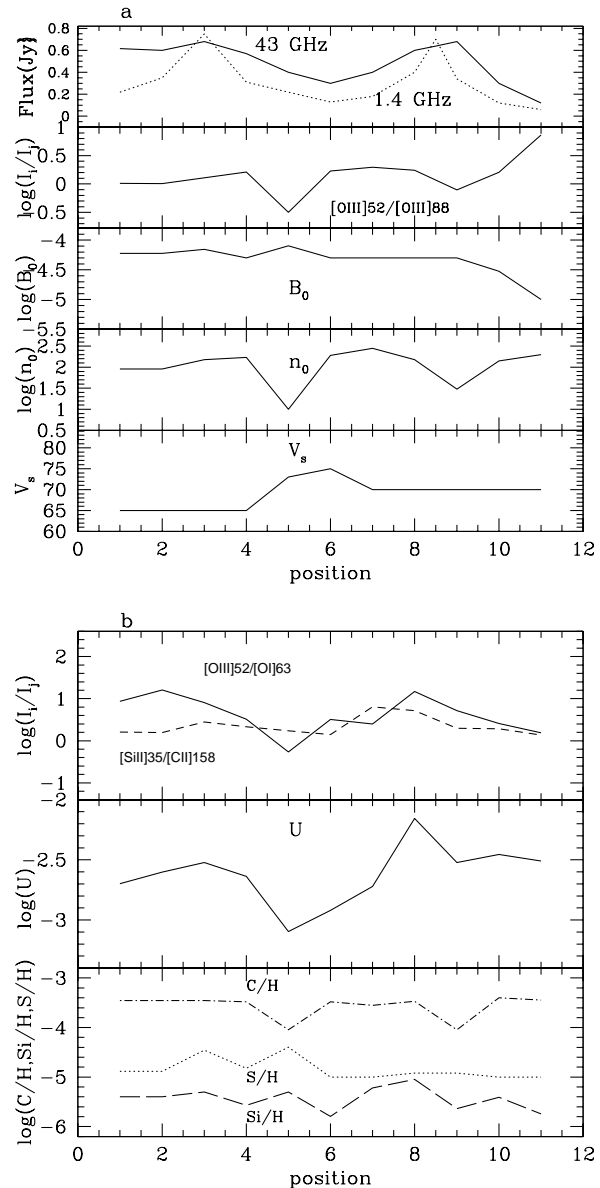


Figure 13. The results along the different positions in the E2-W1 crossing strip. a :the parameters depending on the shock. b : the parameters depending on photoionization and the relative abundances

observed in the radio range from nebulae ionised and heated by radiation from both the stars and shocks. The relative importance of synchrotron radiation to bremsstrahlung determines the non-thermal or thermal character. Fig. 14a shows that the radio datum at 43 GHz can be explained by thermal bremsstrahlung as well as by dust reradiation. If it corresponds to dust reradiation, the synchrotron radiation flux created could also contribute. We do not have enough data in the radio range to confirm this. On the other hand, if the radio flux which refers to the data from Sofue et al. (1987) follows the bremsstrahlung trend, it can indicate some free-free self-absorption towards lower frequencies. For comparison, we have added in Fig. 12a and b the synchrotron power-law radiation flux (long-dashed line) which clearly follows a different trend.

To investigate the continuum for the other positions, we show in Fig. 14b the data in both the IR and radio frequency ranges for all the positions. The results found for position 2 are valid on a large scale also for the other positions. The dust temperatures are now constrained by radio data at 43 GHz. We have thus added the black body flux corresponding to 200 K (black dotted line). Such a dust temperature is easily reached by small grains.

In Fig. 14c, a zoom on the dust reradiation maximum is shown. We can conclude that dust cannot reach temperatures higher than 200 K. In most positions there is an absorption feature at wavelengths $\geq 30 \mu\text{m}$. Even if the data are insufficient to determine the absorption and emission bands of typical grains, we suggest that the feature at $\sim 30 \mu\text{m}$ is not so rare, since it was discovered from ground based observations in 63 Galactic objects : 36 evolved carbon stars, 14 PPNe, and 13 PNe (Hony et al. 2002). In our Galaxy, this feature, whose carrier seems to be MgS species, occurs from extreme AGB stars on to later stages (Jiang et al. 2008).

6 CONCLUDING REMARKS

We have modelled the IR spectra observed in the region near the Galactic center with the aim of determining the physical conditions in the different observed positions. We have obtained the results by comparing the calculated with the observed line ratios and of the continuum SED data. Our models account for the coupled effect of the shocks and the photoionizing flux.

The models are matter-bound, indicating a high degree of fragmentation of matter, that is characteristic of turbulent regimes. We have found that the shocks propagate towards the photoionizing source, i.e. the star clusters, suggesting that gravitation may prevail over eventual wind effects. The shock velocities range between ~ 65 and 80 km s^{-1} . Indeed, they are not high enough to produce X-ray emission by bremsstrahlung (e.g. Fig. 5) and to collisionally heat the dust grains to the observed temperatures of ~ 150 K in some positions of the Arched Filament region and of ~ 88 K in the E2-W1 crossing strip. In the downstream regions, the characteristic electron temperature and density profiles lead to a good agreement of calculated line ratios from different ionization levels, with the observed ones.

The results obtained with pure photoionization models which account on the [OIII] and [SIII] line ratios (e.g. Rodríguez-Fernández et al. 2001, Simpson et al. 2007, etc) demonstrate that photoionization from the clusters affects the intermediate ionization level line ratios. However, adopting the composite models, detailed results can be found also for the shock velocities, pre-shock densities, and pre-shock magnetic fields, by modelling different level lines.

The pre-shock densities range between $\geq 1 \text{ cm}^{-3}$ in the ISM and $\geq 200 \text{ cm}^{-3}$ in the filamentary structures. High densities ($n_0 = 100\text{-}80 \text{ cm}^{-3}$) are found in the Arched Filaments, the maximum values ($n_0 = 200 \text{ cm}^{-3}$) in E91 position C, and in C96 positions 7 and 11 (280 and 200 cm^{-3} , respectively).

The magnetic field ranges from $5 \cdot 10^{-6}$ gauss in S07 positions 1 and 2, characteristic of the ISM, increasing smoothly to $> 5 \cdot 10^{-5}$ gauss beyond the Bubble, up to a

maximum of $8 \cdot 10^{-5}$ gauss. These values are about the same as found in the crossing strip E2-W1 in the Arched Filaments. Beyond the Arched Filaments, B_0 regains the ISM values. Our results confirm LaRosa et al. (2005) predictions of the magnetic field strength.

The maximum temperature of the stars are higher in the Quintuplet Cluster (~ 38000 K) than in the Arches Cluster (~ 27000 K). There are stars at temperatures of ~ 35000 K in the southern ISM and of ~ 39000 K in the northern one, above 0.1 degree. The ionization parameter is relatively low (< 0.01) reaching a maximum of > 0.01 near the Arches Cluster. This indicates that the observed positions 30-35 are closer to the stars. In the E2-W1 strip, U is rather low, diluted by the distance from the ionization source, most probably the Arches Cluster.

The depletion from the gaseous phase of Si is ubiquitous, indicating the presence of silicate dust throughout all the region, while a large quantity of iron rich grains is present in the region of the Arched Filaments.

Comparing the relative abundances for positions 29-34, S07 find the average $\text{Ne}/\text{H} = 1.63 \pm 0.08 \cdot 10^{-4}$, $\text{S}/\text{H} = 1.16 \pm 0.06 \cdot 10^{-5}$, while we find that $\text{Ne}/\text{H} \sim 10^{-4}$ satisfactorily fits all positions and S/H fluctuates between $6.3 \cdot 10^{-6}$ and $1.6 \cdot 10^{-5}$. S07 find $\text{Fe}/\text{H} \sim 1.3 \cdot 10^{-6}$ in the Arched Filament and $\sim 8.8 \cdot 10^{-6}$ in the Bubble, in agreement with our results : $\text{Fe}/\text{H} \sim 10^{-5}$ in the Bubble and 10^{-6} in the Arched Filaments (Fig. 3c).

The continuum SED between 33 and $158 \mu\text{m}$ in all the observed regions indicate that a component of dust heated to temperatures of $\sim 100\text{-}200$ K must be present. The dust grains coupled to gas within the emitting clouds cannot reach those high temperatures by using the input parameters which are constrained by the fit of the line spectra. Higher ionization parameters and small grains characterise this dust. We suggest that hot dust is located closer to the stars than the emitting gaseous clumps. The temperature of the stars is not high enough to destroy the grains by evaporation, and the shock velocity cannot disrupt them totally by sputtering. In the Arched Filaments, we find a dust-to-gas ratio ~ 0.4 by mass.

The data are insufficient to show absorption and emission bands from the grains or to constrain the dust-to-gas ratios in the different regions. PAHs can be present in some Arched filament region positions, leading to a strong absorption of the photoionizing flux from the stars.

The radio emission seems thermal bremsstrahlung in all the positions observed in the Arched Filaments, however a synchrotron radiation component is not excluded. More data should confirm and improve the modelling presented in this paper.

ACKNOWLEDGEMENTS

I am grateful to J. P. Simpson, E. F. Erickson, and S. W. Colgan, for allowing me to reproduce their figures, and to an anonymous referee for many important comments. I thank R. Angeloni for helpful advise.

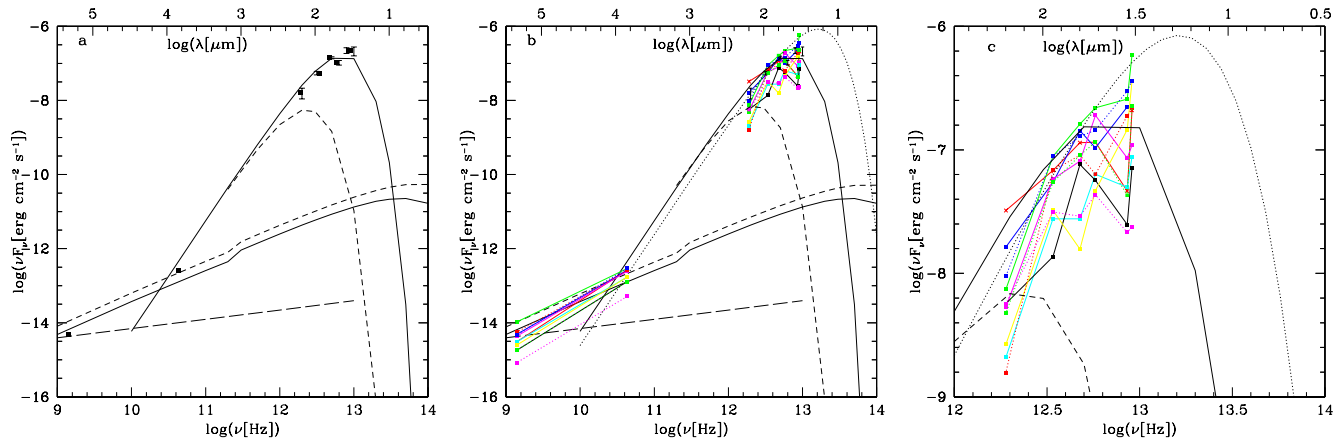


Figure 14. The continuum SEDs in the E2-W1 Strip. a : position 2. short-dashed : model mc2; long-dashed : synchrotron radiation; solid line : model calculated with $U=5$ and $a_{gr}=0.01 \mu\text{m}$. b : the comparison for all position. Solid lines : red : 1; blue : 2; green : 3; magenta : 4; cyan : 5; black : 6; yellow : 7. Dotted lines : red : 8; blue : 9; green : 10; magenta : 11. c : a zoom in the IR maximum. For all models two curves appear referring to the bremsstrahlung and to reradiation by dust

REFERENCES

- Allen, C. W. in *Astrophysical Quantities*. London: The Athlone Press, 1973
- Colgan, S. W. J., Erickson, E. F., Simpson, J. P., Haas, M. R., Morris, M. 1996, *ApJ*, 470, 882
- Contini, M. 1997, *A&A*, 323, 71
- Contini, M. 2004, *MNRAS*, 354, 675
- Contini, M., Contini, T. 2007, *AN*, 328, 953
- Contini, M., Viegas, S.M. 2001, *ApJS*, 132, 211
- Contini, M., Viegas, S. M., Prieto, M. A. 2004, *MNRAS*, 348, 1065
- Cotera, A. S., Erickson, E. F., Colgan, S. W. J., Simpson, J. P., Allen, D. A., Burton, M. G. 1996, *ApJ*, 461, 750
- Cotera, A. S., Colgan, S. W. J., Rubin, R. H., Simpson, J. P. 2005, *ApJ*, 622, 333
- Cox, D. P. 1972, *ApJ*, 178, 143
- Draine, B. T. in "The Cold Universe" : Saas-Fee Advanced Course 32, ed. D.Pfenniger, Berlin : Springer-Verlag, 2003
- Draine, B.T., Li, A. 2007, *ApJ*, 657, 810
- Egan, M. P., Shipman, R. F., Price, S. D., Carey, S. J., Clark, F. O., Cohen, M. 1998, *ApJ*, 494, L199
- Eisenhauer, G. et al. 2005, *ApJ*, 628, 246
- Erickson, E. F., Colgan, S. W. J., Simpson, J. P., Rubin, R. H., Morris, M., Haas, M. R. 1991, *ApJ*, 370, L69
- Figer, D. F.; McLean, I. S.; Morris, M. 1995, *ApJ*, 447, L29
- Figer, D. F., Kin, S. S., Morris, M., Serabyn, E., Rich, R. M., McLean, I. S. 1999, *ApJ*, 525, 750
- Figer, D. F. et al. 2002, *ApJ*, 581, 258
- Genzel, R., Stacey, G. J., Harris, A. I., Townes, C. H., Geis, N., Graf, U. U., Poglitsch, A., Stutzki, J. 1990, *ApJ*, 356, 160
- Ghez, A.M. et al. 2005, *ApJ*, 620, 744
- Hoefner, S. 2009ArXiv0904.2166
- Hony, S., Waters, L.B.F.M., Tielens, A.G.G.M. 2002, *A&A*, 390, 533
- Jiang, B. W., Zhang, Ke, Li, Aigen 2008, *Earth Planets Space*, 60, 1-7
- Kim, S. S., Morris, M., Lee, H. M. 1999, *ApJ*, 525, 228
- Kim, S. S., Figer, D. F., Lee, H. M., Morris, M. 2000, *ApJ*, 545, 301
- Kurucz, R.L. 1979, *ApJS*, 40, 1
- Lacy, J. H., Townes, C. H., Hollenbach, D. J. 1982, *ApJ*, 262, 120
- Lang, C. C.; Goss, W. M.; Morris, M. 2001, *AJ*, 121, 2681
- Lang, C. C.; Johnson, K. E.; Goss, W. M.; Rodríguez, L. F. 2005, *AJ*, 130, 2185
- LaRosa, T. N., Brogan, C. L., Shore, S. N., Lazio, T. J., Kassim, N. E., Nord, M. E. 2005, *ApJ*, 626, L23
- Levine, D., Morris, M., Figer, D. 1999, *ESASP*, 427, 699
- Martín-Hernández, N. L. et al. 2002, *A&A*, 381, 606
- Morris, M., Yusef-Zadeh, F. 1989, *ApJ*, 343, 703
- Morris, M., Davidson, J.A., Werner, M.W. 1995 *ASPC*, 73, 477
- Nagata, T., Woodward, C. E., Shure, M., Kobayashi, N. 1995, *AJ*, 109, 1676
- Oka, T., Hasegawa, T., Sato, F., Tsuboi, M., Miyazaki, A. 2001, *PASJ*, 53, 779
- Osterbrock, D.E. 1988 in *Astrophysics of Gaseous Nebulae and Active Galactic Nuclei*, University Science Book
- Price, S. D.; Egan, M.P., Carey, S. J., Mizuno, D. R., Kuchar, T. A. 2001, *AJ*, 121, 2819
- Rodríguez-Fernández, N. J., Martín-Pintado, J., Fuente, A., de Vicente, P., Wilson, T. L., Hüttemeister, S. 2001, *A&A*, 365, 174
- Serabyn, E.; Guesten, R. 1991, *A&A*, 242, 376
- Schödel, R. Bower, G.C., Muno, M.P., Nayakshin, S., Ott, T. 2006, *Journal of Physics: Conference Series*, Volume 54, Proceedings of "The Universe Under the Microscope - Astrophysics at High Angular Resolution", held 21-25 April 2008, in Bad Honnef, Germany. Editors: Rainer Schoedel, Andreas Eckart, Susanne Pfalzner and Eduardo Ros, pp. (2006).
- Simpson, J. P., Colgan, S. W. J., Cotera, A. S., Erickson, E. F., Haas, M. R., Morris, M., Rubin, R. H. 1997, *ApJ*, 487, 689
- Simpson, J.P., Rubin, R.H., Colgan, S.W., Erickson, E.F., Haas, M.R. 2004, *ApJ*, 611, 338
- Simpson, J. P.; Colgan, S. W. J., Cotera, A. S., Erickson, E. F., Hollenbach, D. J., Kaufman, M. J., Rubin, R. H. 2007, *ApJ*, 670, 1115

- Sofue, Y; Reich, W., Inoue, M., Seiradakis, J. H. 1987, PASJ, 39, 95
- Timmermann, R., Genzel, R., Poglitsch, A., Lutz, D., Madden, S. C., Nikola, T., Geis, N., Townes, C. H. 1996, ApJ, 466, 242
- Tsuboi, M., Inoue, M., Handa, T., Tabara, H., Kato, T. 1985, PASJ, 37, 359
- Yusef-Zadeh, F., Morris, M. 1987, ApJ, 320, 557
- Yusef-Zadeh, F., Morris, M. 1988, ApJ, 329, 729
- Yusef-Zadeh, F., Morris, M., Chance, D. 1984, Nature, 310, 557
- Yusef-Zadeh, F., Law, C., Wardle, M. 2001, AAS, 19910902
- Yusef-Zadeh, F.; Law, C.; Wardle, M.; Wang, Q. D.; Fruscione, A.; Lang, C. C.; Cotera, A. 2002, ApJ, 570, 665